

Speg interactions that regulate the stability of excitation-contraction coupling protein complexes in triads and dyads

Chang Seok Lee^{1,5}, Sung Yun Jung^{2,5}, Rachel Sue Zhen Yee¹, Nadia H. Agha¹, Jin Hong¹, Ting Chang¹, Lyle W. Babcock¹, Jorie D. Fleischman¹, Benjamin Clayton¹, Amy D. Hanna¹, Christopher S. Ward¹, Denise Lanza³, Ayrea E. Hurley¹, Pumin Zhang⁴, Xander H. T. Wehrens¹, William R. Lagor¹, George G. Rodney¹ & Susan L. Hamilton¹✉

Here we show that striated muscle preferentially expressed protein kinase α (Speg α) maintains cardiac function in hearts with Speg β deficiency. Speg is required for stability of excitation-contraction coupling (ECC) complexes and interacts with esterase D (Esd), Cardiomyopathy-Associated Protein 5 (Cmya5), and Fibronectin Type III and SPRY Domain Containing 2 (Fsd2) in cardiac and skeletal muscle. Mice with a sequence encoding a V5/HA tag inserted into the first exon of the *Speg* gene (HA-Speg mice) display a >90% decrease in Speg β but Speg α is expressed at ~50% of normal levels. Mice deficient in both Speg α and Speg β (Speg KO mice) develop a severe dilated cardiomyopathy and muscle weakness and atrophy, but HA-Speg mice display mild muscle weakness with no cardiac involvement. Speg α in HA-Speg mice suppresses Ca²⁺ leak, proteolytic cleavage of Jph2, and disruption of transverse tubules. Despite its low levels, HA-Speg β immunoprecipitation identified Esd, Cmya5 and Fsd2 as Speg β binding partners that localize to triads and dyads to stabilize ECC complexes. This study suggests that Speg α and Speg β display functional redundancy, identifies Esd, Cmya5 and Fsd2 as components of both cardiac dyads and skeletal muscle triads and lays the groundwork for the identification of new therapeutic targets for centronuclear myopathy.

¹Department of Integrative Physiology, Baylor College of Medicine, Houston, TX 77096, USA. ²Department of Biochemistry, Baylor College of Medicine, Houston, TX 77096, USA. ³Department of Molecular and Human Genetics, Baylor College of Medicine, Houston, TX 77096, USA. ⁴The First Affiliated Hospital, Zhejiang University Medical School, Hangzhou, China. ⁵These authors contributed equally: Chang Seok Lee, Sung Yun Jung. ✉email: susanh@bcm.edu

Centronuclear myopathies (CNM) are congenital myopathies characterized by centralized nuclei in myofibers and muscle weakness that ranges from mild to life-threatening¹. CNM is associated with X-linked recessive mutations in *MTM1* (Myotubularin 1) and autosomal mutations in *DNM2* (Dynamin 2), *BINI1* (Bridging Integrator 1), *RYR1* (Ryanodine Receptor 1), *CACNA1S* (Calcium Voltage-Gated Channel Subunit Alpha1 S), *TTN* (Titin), and *SPEG* (Striated Muscle Preferentially Expressed Protein Kinase)¹. Bin1, Dnm2, and Mtm1 play critical roles in transverse tubule (t-tubule) formation and structure^{1–9}. Mtm1, a lipid phosphatase, regulates the activities of PI3 kinase, Dnm2, and Bin1¹⁰. T-tubules in skeletal and cardiac muscle are invaginations of the sarcolemma that form dyads and triads with the sarcoplasmic reticulum in cardiac muscle and skeletal muscle, respectively. These structures are essential for excitation-contraction coupling (ECC) in striated muscle. RyR1, which is the skeletal muscle Ca²⁺ release channel, and the dihydropyridine receptor (DHPR or Ca_v1.1), which is a voltage-dependent Ca²⁺ channel (α1s subunit encoded by *CACNA1S*), are critical for ECC and localized to triads. Their counterparts in cardiac tissue, RyR2, and Ca_v1.2, are localized to dyads. Speg interacts with RyR2^{11,12}, Serca2a¹³, and Jph2¹² in the heart and Mtm1¹⁴, Dnm2¹⁵, and desmin¹⁰ in skeletal muscle, suggesting that Speg plays roles in both ECC and t-tubule organization. Collectively, these data suggest that CNM arises from the disruption of t-tubules and triadic/dyadic ECC complexes.

ECC is the process whereby an action potential activates Ca_v1.2 opening (cardiac) or causes a Ca_v1.1 conformational change (skeletal muscle) to trigger the opening of SR Ca²⁺ release channels (RyR2 and RyR1, in heart and skeletal muscle, respectively), leading to muscle contraction¹⁶. The composition of the ECC complex has been studied for many years with proteins such as Ca²⁺ release channels (RyR1 and RyR2)^{17–19}, junctophilins (Jph1 and 2)^{20–23}, triadin^{24–26}, junctin^{27,28}, FK506 binding proteins (Fkbp12 and Fkbp12.6)^{29–31}, Stac3^{32–34}, and calmodulin^{35–38} identified as key components. More recently, Speg^{6,10–12,14,15,39–42} and cardiomyopathy-associated 5 protein or myospryn (Cmya5)⁴³ have been identified as part of the ECC complex in cardiac and skeletal muscle, but their functional roles remain to be fully elucidated.

Speg is a member of the myosin light chain kinase (MLCK) protein family^{1,6} with two kinase domains similar to those of the muscle giant protein obscurin. In striated muscle, Speg is expressed as two alternatively spliced isoforms: Spegα (250 kDa) and Spegβ (355 kDa), differing at the N-terminus due to different transcriptional initiation sites. Both Speg isoforms have multiple Ig and FnIII domains that allow them to interact with other proteins and possibly position their binding partners for phosphorylation. Agrawal et al.¹⁴ found that Speg protein levels were severely depleted in patients with *Speg* mutations associated with CNM and suggested that Speg-deficient mice are good models for CNM. Huntoon et al.³⁹ created striated muscle-specific Speg-KO mice, which developed dilated cardiomyopathy and severe skeletal muscle myopathy. The skeletal muscle of these Speg-deficient mice displayed a reduced ability to generate force, abnormal triads, decreased Ca_v1.1-mediated Ca²⁺ currents, decreased SR Ca²⁺ release, altered ECC³⁹ and a deficiency in satellite cells⁴⁰. Quick et al.¹² used tamoxifen-inducible cardiomyocyte-specific Speg-deficient mice to demonstrate that Speg deficiency in the heart causes heart failure (HF) associated with increased SR Ca²⁺ spark frequency and disruption of the t-tubules. Agrawal and colleagues³⁹ demonstrated spatial variability in electrically evoked Ca²⁺ transients in Speg-KO skeletal muscle fibers, reminiscent of Mtm1 deficiency⁴⁴. Recently, Li et al.¹⁵ found that decreasing the expression of Dnm2 in Speg-deficient mice improved skeletal but not cardiac muscle function in Speg-deficient mice.

Campbell et al.¹¹ identified S2367 as a Speg phosphorylation site on RyR2 and demonstrated that conversion of S2367 to an alanine to prevent phosphorylation promoted atrial fibrillation, while conversion to an aspartic acid to mimic phosphorylation prevented pacing-induced atrial fibrillation. Speg phosphorylation sites on RyR1 have not been identified, and the sequence, including S2367 in RyR2, is not conserved in RyR1.

Another likely target of Speg phosphorylation is Jph2, a protein that is essential for maintaining dyads²³ and t-tubules⁴⁵ in cardiac muscle. Abnormal t-tubules and disrupted dyads are associated with cardiac hypertrophy and heart failure²³. Jph2 is the primary isoform expressed in cardiac muscle, and both Jph1 and Jph2 are expressed in skeletal muscle. The site of Speg phosphorylation of Jph2 has not yet been identified, but phosphorylation of this protein at structural motifs could have profoundly different functional outcomes. Junctophilins have eight N-terminal MORN (membrane occupation and recognition nexus) repeats, of which the first three interact with the voltage-dependent Ca²⁺ channel (Ca_v1.1 or Ca_v1.2)⁴⁶. The MORN repeats form a continuous β sheet and are followed by a long helix that serves as a backbone for the sheet. The C-terminal domain interacts with the SR membrane and, possibly, with RyRs⁴⁷. Jph2 is cleaved by calpains in response to increased cytosolic Ca²⁺ levels, and an N-terminal fragment of Jph2 in the heart translocates to the nucleus, where it serves as a stress-activated transcription factor^{48–50}. A mutation in the joining domain between the 6th and 7th MORN domains causes disruption of the dyads⁵¹. This joining domain interacts with Ca_v1.2 to recruit it to the t-tubules⁵¹. Mutations and deficiencies in RyRs, Speg^{11,12,39}, Jph2^{43,52}, and Cmya5⁴³ (myospryn/TRIM76) cause abnormal t-tubules, aberrant SR Ca²⁺ release, and cardiac and/or skeletal muscle dysfunction^{43,52,53}, but the details of how these proteins structurally and functionally interact remain to be fully elucidated.

In this manuscript, we describe a mouse model that expresses Spegβ with an HA-Tag (HA-Speg mice). These mice display a significant decrease in Spegβ and a lesser decrease in Spegα (not HA-tagged) protein levels. We compared the effects of Speg deficiencies in Speg-KO (MCK-Cre⁺*Speg*^{fl/fl}) and HA-Speg mice on Ca²⁺ spark frequency and t-tubule disruption to show that Ca²⁺ leak occurs in areas of t-tubule disruption. We also evaluate the effects of Speg deficiency on the levels of ECC proteins, Jph2 fragmentation, and interactions among triadic and dyadic proteins and relate these changes to functional differences between HA-Speg and Speg-KO mice. We use HA-Speg mice to confirm RyRs and Jph2 as Speg-binding proteins and to identify new interacting proteins, including Esd, Cmya5 and Fsd2, in both heart and skeletal muscle. We use BioID with Fkbp12-BirA to show that these currently identified Speg-binding proteins localize to the triads in skeletal muscle and, using RyR and Jph2 immunoprecipitations, we confirm that Esd, Cmya5, and Fsd2 are Speg-dependent components of RyR/Jph2 triadic and dyadic complexes and that the absence of Speg leads to destabilization of triadic and dyadic ECC protein complexes. Our study shows that the severity of the disease associated with Speg deficiency correlates with t-tubule disruption, increased Ca²⁺ spark frequency in regions of t-tubule disruption, decreased ECC proteins, Jph2 fragmentation, and disruption of ECC protein complexes, and that a deficiency in Spegβ is partially rescued by Spegα.

Results

Creation of HA-Speg mice and comparison with Speg-KO mice. Because of difficulties encountered with Speg immunoprecipitation using several currently available Speg antibodies, we created a mouse model to identify Speg-binding partners. Using CRISPR/Cas9-mediated genome editing to insert a sequence

encoding a V5 (a 14 amino acid sequence from simian virus⁵⁴) combined with a 3XHA tag (9 amino acid sequence from influenza virus hemagglutinin) (Supplementary Fig. 1) into the *Speg* gene, we created mice with the V5/HA-tagged *Speg* β (HA-*Speg* mice) to use for identification of *Speg*-binding proteins. Since the sequence encoding the tag is inserted in the first exon of *Speg* β , only *Speg* β has the V5/HA-tag. The heterozygous mice were backcrossed with wild-type mice at least twice to reduce off-target effects of the editing, and then the heterozygous mice were crossed to produce homozygous HA-*Speg* β mice. The insertion of the V5/HA-tag decreased *Speg* β and *Spega* protein levels in the *tibialis anterior* (TA) muscle of homozygous HA-*Speg* mice by $95.1 \pm 0.8\%$ (mean \pm SD) and $50.9 \pm 8.7\%$, respectively (Fig. 1a), and, in the heart, *Speg* β and *Spega* levels were reduced by $82.1 \pm 4.2\%$ and $38.3 \pm 6.7\%$, respectively (Fig. 1c). Hence, we have created a mouse model of *Speg* β deficiency with some sparing of *Spega*. In contrast, MCK-Cre⁺*Speg*^{fl/fl} mice¹¹ (driven by the muscle creatine kinase promoter, which we designate as *Speg*-KO mice) display a >95% decrease in both *Speg* β and *Spega* in both skeletal muscle (Fig. 1b) and heart (Fig. 1d).

To elucidate the cause(s) of the reduction in *Speg* isoforms in HA-*Speg* mice, we measured relative mRNA levels for *Speg* β , *Spega*, and two splice variants of the *Speg* gene, *Apeg*, and *Bpeg* in skeletal and cardiac muscle. As can be seen in Fig. 1e, only the message for *Speg* β was decreased in the muscle of HA-*Speg* mice and showed a tendency toward a decrease in the heart (Fig. 1f). mRNA levels for *Spega*, *Apeg*, and *Bpeg* were not significantly altered. It seems unlikely that a 50% decrease in mRNA would lead to a 95% decrease in *Speg* β levels. However, the 3xHA tag has been shown to cause increased proteolytic degradation of a variety of different tagged proteins⁵⁵, suggesting that some of the decrease in HA-*Speg* β are likely due to protein turnover. Since *Speg* β and *Spega* have identical C-terminal sequences, we cannot use mass spectrometry to distinguish between the two isoforms using immunoprecipitation of *Speg*. However, in HA-*Speg* mice, only *Speg* β has the HA-tag, but the HA antibody coimmunoprecipitates a second band with the MW of *Spega* that is recognized by the *Speg* antibody but not HA antibody (Fig. 1g), suggesting that some *Spega* is bound to *Speg* β . The HA-tag on *Speg* β may render *Spega* complexed to HA-*Speg* β vulnerable to turnover.

ECC protein levels have been reported to be reduced in the skeletal muscle of *Speg*-deficient mice¹⁰, and, hence, quantitation of changes in ECC protein levels is needed to interpret functional and immunoprecipitation data. We compared the effects of *Speg* deficiency on RyR1 and *Cacna1s* (*Ca_v1.1a1s*) and RyR2 and *Cacna1c* (*Ca_v1.2a1c*) protein levels in the TA muscle and heart, respectively, of both HA-*Speg* and *Speg*-KO mice relative to controls (wild type, WT, for HA-*Speg* and *Speg*^{fl/fl} for the *Speg*-KO). RyR1 and *Ca_v1.1a1* were reduced by $34 \pm 7\%$ and $50 \pm 7\%$, respectively, in the skeletal muscle of HA-*Speg* mice compared to control mice (Fig. 1h) and by $83 \pm 4\%$ and $65 \pm 9\%$, respectively, in the TA muscle of *Speg*-KO mice versus control mice (Fig. 1i). Neither RyR2 nor *Ca_v1.2a1c* were reduced in the hearts of either HA-*Speg* (Fig. 1j) or *Speg*-KO mice (Fig. 1k). Hence, while decreased ECC proteins may contribute to the altered skeletal muscle function, a different mechanism appears to underlie the cardiac phenotype.

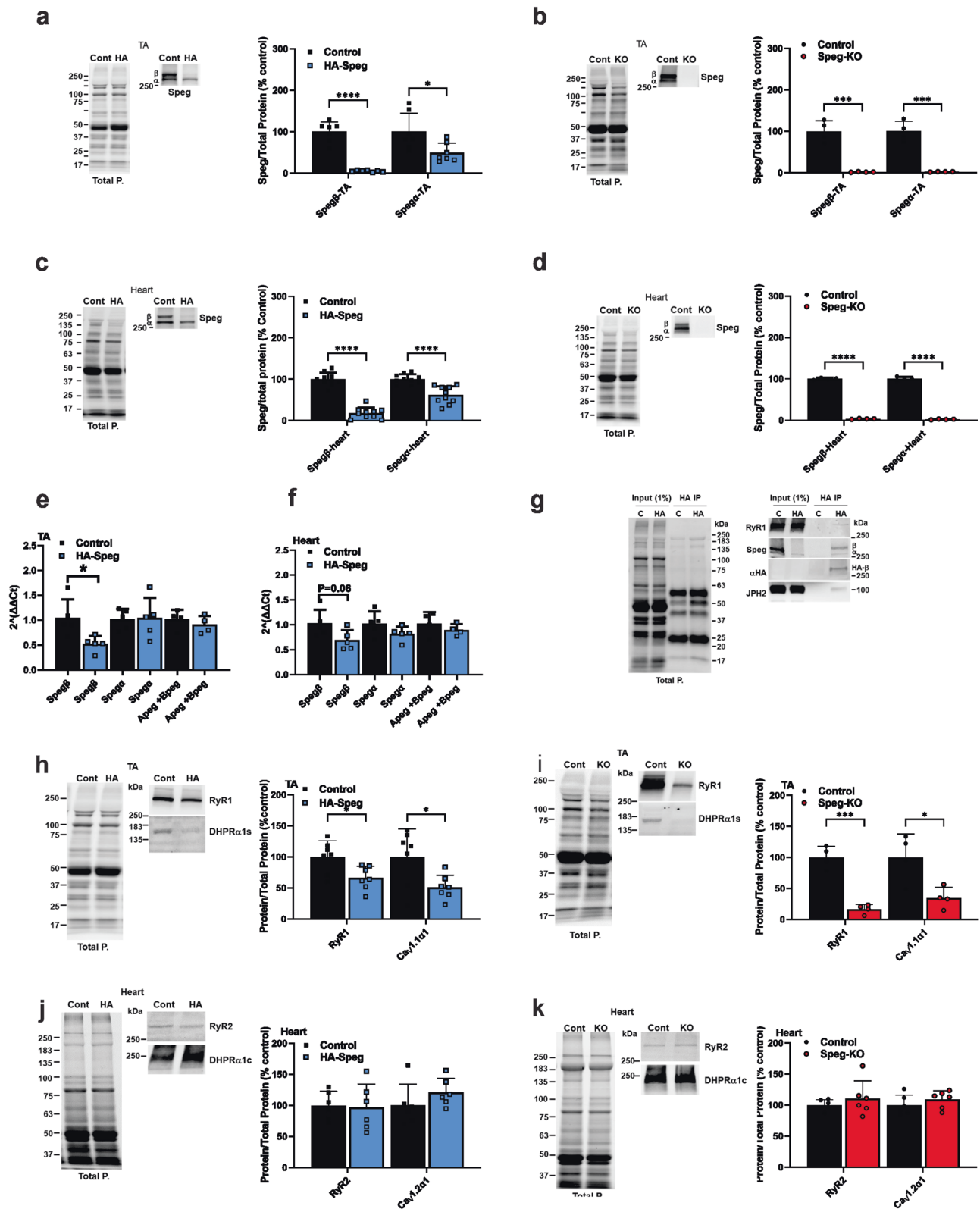
Functional consequences of *Speg* deficiency in *Speg*-KO and HA-*Speg* mice. To evaluate the functional consequences of the reductions in *Speg* in HA-*Speg* compared to *Speg*-KO mice, we performed several functional tests on HA-*Speg* mice compared to control (WT) mice. Similar analyses were performed with the *Speg*-KO and control (*Speg*^{fl/fl}) mice. Neither male nor female HA-*Speg* mice developed dilated cardiomyopathy

(Supplementary Table 1), nor did they not die prematurely. Consistent with published results^{14,39}, both male and female *Speg*-KO mice developed a dilated cardiomyopathy (DCM) (Supplementary Table 1). These data suggest that: (1) smaller amounts of *Speg* β in HA-*Speg* mice are adequate to support cardiac function, (2) *Spega* can compensate for the loss of *Speg* β and/or, (3) *Spega* rather than *Speg* β prevents the development of DCM. The HA-*Speg* male mice were slightly smaller than the age-matched WT (control) mice and had less lean mass (Supplementary Table 2). Both male and female *Speg*-KO mice displayed significant decreases in body weight, length, bone area, fat weight, lean weight, bone mineral concentration (BMC), and bone mineral density (BMD) (Supplementary Table 2).

Ex vivo force generation was reduced in the soleus (Fig. 2a) and the diaphragm (Supplementary Fig. 2a), but not in the *extensor digitorum longus* (EDL) (Fig. 2b) of HA-*Speg* mice. The force-frequency curves were significantly right-shifted by 4.1, 0.7, and 6.0 Hz for the soleus, EDL, and diaphragm muscles, respectively, of male HA-*Speg* mice compared to WT controls (Fig. 2a, b and Supplementary Fig. 2a). For comparison, muscles from male *Speg*-KO mice were more severely affected than those from HA-*Speg* mice, especially the EDL. Maximal force generation was decreased in the soleus (Fig. 2c), EDL (Fig. 2d), and diaphragm (Supplementary Fig. 2b) of the *Speg*-KO male mice. The force-frequency curves were also shifted to the right by an average of 17, 59, and 24 Hz in the soleus, EDL, and diaphragm muscles, respectively, of the *Speg*-KO male mice compared to controls. This rightward shift in the half-maximal stimulation frequency detected in all muscles in the *Speg*-KO mice is likely to be the result of the disruption or inhibition of ECC and/or t-tubules and triads.

Similar experiments were performed with female mice. Maximal force was not significantly decreased in the soleus (Supplementary Fig. 2c) or EDL (Supplementary Fig. 2d) of the female HA-*Speg* mice, but maximal force in the diaphragm of the female HA-*Speg* mice was significantly decreased compared to WT controls (Supplementary Fig. 2e). Maximal force was reduced in the soleus (Supplementary Fig. 2f), EDL (Supplementary Fig. 2g) and diaphragm (Supplementary Fig. 2h) of the female *Speg*-KO mice compared to controls. The half-maximal stimulation frequency was shifted by ~6 Hz in the diaphragm of the female HA-*Speg* mice and by an average of 26, 45, and 22 Hz for the soleus, EDL, and diaphragm muscles, respectively, of *Speg*-KO female mice compared to controls. Hence, *Speg* deficiency has similar effects in male and female mice.

We evaluated the effects of *Speg* deficiency in male HA-*Speg* and *Speg*-KO mice on the cross-sectional area (CSA) and fiber-type distribution of muscle fibers in the soleus and EDL using MyoSight⁵⁶. We found no significant differences in CSA in Type I, IIa, or IIx in the soleus (Fig. 2e, i) or EDL (Fig. 2f, j) of the HA-*Speg* compared to controls. However, the CSA of IIx fibers was reduced in the soleus of *Speg*-KO mice compared to controls (Fig. 2g, k), and the CSA of all fiber types were dramatically reduced in the EDL (Fig. 2h, l). While there were no significant changes in fiber-type distribution in soleus (Fig. 2m) or EDL (Fig. 2n) of HA-*Speg* mice, there was a significant decrease in the % of IIx fibers in soleus (Fig. 2o) of *Speg*-KO mice. The EDL of *Speg*-KO mice displayed a decrease in the percentage of IIa fibers and an increase in the % of IIb fibers (Fig. 2p). CSA distributions for each type of fiber are shown in Supplementary Fig. 3. Based on these analyses, decreased muscle fiber size and fiber-type switching are major features of the *Speg*-KO but not HA-*Speg* mice. Also, our ex vivo force measurements and fiber typing studies show that fast twitch muscles are affected to a much greater extent by *Speg* deficiency than slow twitch muscles, and both male and female mice are affected in *Speg*-KO mice.



Effects of Speg deficiency on SR Ca^{2+} leak and t-tubule structure. Normally, RyR1 opening is tightly controlled by the dihydropyridine receptor (DHPR, $Ca_v1.1$) within the triads of fully differentiated skeletal muscle, and this control serves to suppress spontaneous Ca^{2+} release (Ca^{2+} sparks)⁵⁷. Huntoon et al.³⁹ showed that Speg deficiency promoted spatial variability in macroscopic Ca^{2+} transients and disrupted triads in skeletal

muscle fibers. We examined the t-tubule structure in dissociated *flexor digitorum brevis* muscle (FDB) fibers from HA-Speg, Speg-KO, and control mice. There were areas of abnormal t-tubules in FDB fibers from HA-Speg mice (Fig. 3a, b), but the occurrence of these disruptions was rare. This is in sharp contrast to the FDB fibers from the Speg-KO mice (Fig. 3e, f), where most t-tubules were aberrant. Our findings in the Speg-KO are consistent with

Fig. 1 Speg and ECC protein expression levels in the TA and cardiac muscle of male HA-Speg and Speg-KO mice. **a** Speg β and Speg α expression in the TA of HA-Speg mice (homozygous) compared to controls (WT) ($n = 7$). A representative western blot is shown on the left. Total protein (in all panels) was obtained using stain-free gels (Bio-Rad), and after transfer of the proteins to the PVDF membrane (Immobilon[®]-FL, Millipore), the PVDF membrane was imaged by using a ChemiDoc[™] MP imaging system (Bio-Rad). **b** Speg β and Speg α expression in the TA of Speg-KO mice (homozygous) compared to controls (Speg^{fl/fl}) ($n = 4$ each). A representative western blot is shown on the left. **c** Speg β and Speg α expression in hearts of HA-Speg mice compared to control mice ($n = 10$ each). A representative western blot is shown on the left. **d** Speg β and Speg α expression in the hearts of Speg-KO mice (homozygous) compared to controls (Speg^{fl/fl}) ($n = 4$ each). A representative western blot is shown on the left. **e** Expression of mRNA for Speg α , β , Apeg-1 + Bpeg in TA muscles of control ($n = 4$ –5) and HA-tagged Speg mice ($n = 4$ –5), respectively. P values are indicated as analyzed by Welch's t test. All statistical tests are two-sided. Data are represented as mean \pm standard deviation. **f** Expression of mRNA for Speg β , Speg α , Apeg-1, and Bpeg in hearts of control ($n = 4$ –5) and HA-tagged Speg mice ($n = 4$ –5), respectively. P values are indicated as analyzed by Welch's t test. All statistical tests are two-sided. **g** Immunoprecipitation with HA antibody of homogenate from HA-Speg and control mice. The figure shows western blot of total proteins and western blot with Speg antibody and HA antibody. **h** ECC protein levels in the TA of Speg-KO mice compared to controls with a representative western blot ($n = 7$ each). **i** ECC protein levels in TA of Speg-KO mice compared to controls with a representative western blot ($n = 4$ each). **j** ECC protein levels in the hearts of Speg-KO mice compared to controls with a representative western blot ($n = 6$ each). **k** ECC protein levels in hearts of Speg-KO mice compared to controls with a representative western blot ($n = 6$ each). All mice used for the data in this figure were male. Data are shown as the mean \pm SD. **** $P < 0.0001$, *** $P < 0.001$, ** $P < 0.01$, * $P < 0.05$.

the findings of Huntoon et al.³⁹, with most fibers from the Speg-KO having an abnormal t-tubule structure. T-tubule disorganization ranged from the absence of t-tubules within areas of the myofiber to t-tubule expansion/vacuolation. Using dual imaging of t-tubules (FM4-64) and Ca²⁺ (Fluo-4), we found a significant increase in spontaneous Ca²⁺ sparks in both HA-Speg (Fig. 3c) and Speg-KO fibers (Fig. 3g) and that the Ca²⁺ sparks were located primarily in microdomains of t-tubule disruption in fibers from both HA-Speg (Fig. 3b) and Speg-KO (Fig. 3f). The appearance of Ca²⁺ sparks in adult muscle is likely to be a sign of disruption of Ca_v1.1-RyR1 coupling. T-tubules in areas of spontaneous Ca²⁺ sparks showed structural disorganization, with increased density of longitudinal tubules and decreased transverse tubules, regularity, and integrity (Fig. 3d, h). These findings raise the question of whether increased Ca²⁺ sparks (due to altered phosphorylation of RyRs and/or altered interactions within the triadic ECC complex) activate calpain to cleave Jph2 and disrupt t-tubules or whether the disruption of the t-tubules by the loss of another Speg-dependent pathway (possibly the loss of Jph2 phosphorylation or its interactions with other ECC proteins) alters the structure of the triads/dyads, causing an increase in Ca²⁺ sparks. The two events together are likely to drive a feed-forward, amplifying effect of Speg deficiency with neither change alone being adequate to drive the triadic disruption.

Jph2 fragmentation in HA-Speg and Speg-KO mice. Since HA-Speg mice have a much milder phenotype than Speg-KO mice, a major goal of this study was to compare HA-Speg and Speg-KO mice to find potential pathways where the level of Speg α +Speg β is critical to the phenotype. Since Jph2 and its calpain-mediated cleavage play a critical role in t-tubule and triad structure^{5,39}, we evaluated the extent of Jph2 cleavage in the two mouse models to determine if Jph2 levels and cleavage were different in the two mouse models of Speg deficiency.

Jph2 levels in the heart are downregulated by cardiac stress^{58–60}, and the decrease is, at least partially, due to calpain cleavage of Jph2 into fragments^{49,50,61,62}. Junctophilins are required for the maintenance of the structure of skeletal muscle triads and cardiac dyads⁶³. Based on the Jph2 sequence, Jph2 should have a molecular weight (MW) of 75 kDa, but it migrates on sodium dodecyl sulfate (SDS) polyacrylamide gel electrophoresis (PAGE) with an apparent MW of ~101 kDa (Fig. 4a, green Ab J2-431-680). Jph1 (MW of 72 kDa) migrates in SDS-PAGE with an apparent MW of 87 kDa (Fig. 4a, red J1-Ab 559-572). Full-length Jph2 is labeled as band a in Fig. 4b, d, f, h. The anomalous migration of junctophilins on SDS gels could be due to posttranslational modifications such as palmitoylation⁶⁴,

interactions with other proteins that are not disrupted by SDS, or an unusual conformation of the partially unfolded Jph. The protein levels of full-length Jph2 were reduced by 28 \pm 10% in the tibialis anterior (TA) muscle of HA-Speg mice (Fig. 4b, c) and by 45 \pm 9% in the TA muscle of Speg-KO mice (Fig. 4d, e). Jph2 was reduced by 32 \pm 20% in the hearts of HA-Speg mice (Fig. 4f, g) and by 55 \pm 6% in the hearts of Speg-KO mice (Fig. 4h, i). Hence, both models of Speg deficiency display a decrease in skeletal muscle and heart levels of Jph2, with the decreases being greater in Speg-KO mice.

The anomalous migration of both Jph2 and Jph1 makes it extremely difficult to estimate the size of the Jph2 fragments and/or identify calpain cleavage sites. Weninger et al.⁶² identified calpain cleavage sites on recombinant Jph2 (which migrated as a >100 kDa protein) and ordered the sites sequentially using increasing concentrations of calpain⁶². Sequentially, calpain was suggested to cleave Jph: (1) after arginine 565 (in agreement with Guo et al.⁵⁰), (2) after serine 164, (3) between amino acids 235 and 297, and (4) between 590 and 612⁶². While this study identified sites that can be cleaved by calpain in the context of recombinant Jph2, calpain cleavage sites on Jph2 in cardiac or skeletal muscle could be masked by protein-protein interactions or Jph2 posttranslational modifications (e.g., phosphorylation, palmitoylation). Guo et al.⁶⁵ identified calpain cleavage sites at Val-155/Arg-156, Leu-201/Leu-202, and Arg-565/Thr-566.

Our goal was to determine if Speg deficiencies in our two mouse models had similar effects on Jph2 cleavage. To identify Jph2 fragments in TA and cardiac muscle homogenates HA-Speg and Speg-KO mice compared to their controls using western blotting, we employed three validated sequence-specific antibodies (Fig. 4j): (1) an antibody to Jph2 amino acids 1–50 (J2-1-50). (2) an antibody to Jph2 amino acids 431–680 (J2-431-680), and (3) an antibody to Jph2 amino acids 565–580 (J2-565-580), which is immediately after the first putative calpain cleavage site⁶². The fragmentation patterns in western blot panels using these antibodies for the TA of HA-Speg mice are shown in Fig. 4b, c. The Jph2 fragments in the Speg TA of Speg-KO mice are shown in Fig. 4d, e. The Jph2 fragments identified in Fig. 4d as bands a–d are explained in Fig. 4j and quantified in Fig. 4e. Full-length Jph2 is band a in Fig. 4 and is recognized by all three antibodies. While full-length Jph2 (band a) was decreased in the TA muscle of both the HA-Speg and Speg-KO mice, none of the proteolytic fragments in the TA of HA-Speg mice increased compared to controls. Instead, the 91 kDa (band b) and the 28 kDa (band d) fragments actually displayed small decreases (Fig. 4c, d). Three bands were increased in the TA muscle of Speg-KO mice including a 91 kDa (band b), a 70 kDa (band c),

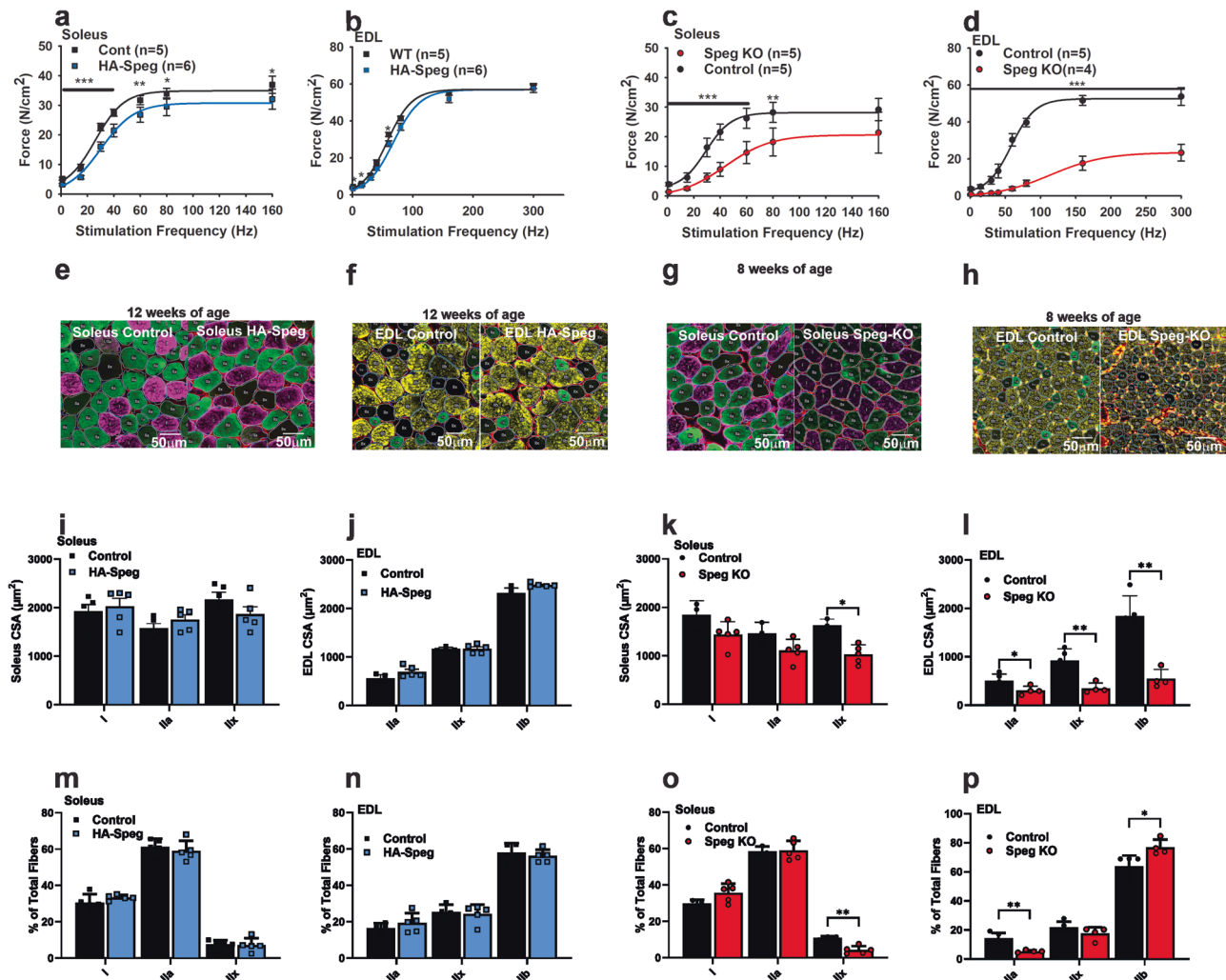
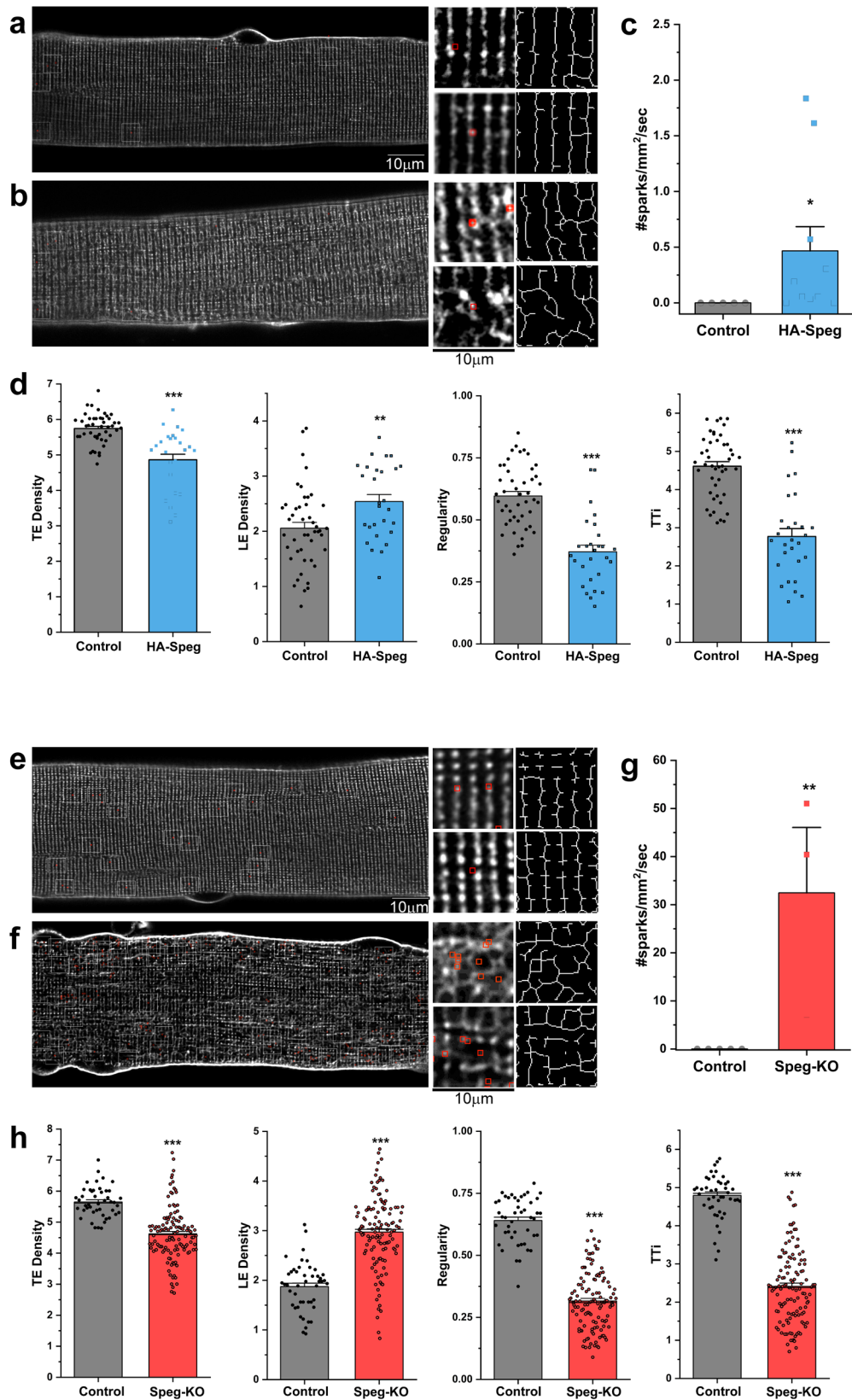


Fig. 2 Functional consequences of *Speg* deficiency. Skeletal muscle function in HA-Speg (14 weeks), WT (13 weeks), *Speg*-KO (8–9 weeks), and *Speg*^{fl/fl} (8–9 weeks) male mice were assessed using the indicated skeletal muscle functional or structural measurements. All data in this figure were obtained with male mice. Data on the diaphragm and separate data on female mice of each genotype are provided in the Supplementary Data Fig. 2. The *Speg*-KO mice used were younger than HA-Speg mice because they become extremely sick at ~10 weeks of age and often do not survive the echoes. **a** Force-frequency data for control (WT) and HA-Speg soleus. **b** Force-frequency data for the control (WT) and HA-Speg EDL. **c** Force-frequency data for control and *Speg*-KO soleus. **d** Force-frequency data for control and *Speg*-KO EDLs. **e** Fiber-type-specific staining of a representative cross-section from the soleus of control and HA-Speg mice. **f** Fiber-type-specific staining of a representative cross-section from the soleus of control and *Speg*-KO mice. **g** Fiber-type-specific staining of a representative cross-section from the EDL of control and *Speg*-KO mice. **h** Fiber-type-specific staining of a representative cross-section from the EDL of control and *Speg*-KO mice. **i** Average CSA of different fiber types in the soleus of control and HA-Speg mice. **j** Average CSA of different fiber types in the EDL of control and HA-Speg mice. **k** Average CSA of different fiber types in the soleus of control and *Speg*-KO mice. **l** Average CSA of different fiber types in the EDL of control and *Speg*-KO mice. **m** Fiber-type distribution in the soleus of control and HA-Speg mice. **n** Fiber-type distribution in the EDL of control and HA-Speg mice. **o** Fiber-type distribution in the soleus of control and *Speg*-KO mice. **p** Fiber-type distribution in the EDL of control and *Speg*-KO mice. Data are plotted as the mean ± SD. ****P < 0.0001, ***P < 0.001, **P < 0.01, and *P < 0.05.

and a 28 kDa (band d) (Fig. 4d, e). The 91 kDa fragment (band b) was recognized by J2-431-680 and J2-565-580, but not by the N-terminal (J2-1-50) antibody, suggesting a *Speg*-protected cleavage site close to the N-terminus. The N-terminal antibody also recognized a 85 kDa band, but this band was not detected by any other *Jph2* antibody and was not different between controls and *Speg*-KO muscle and is, hence, likely to represent a nonspecific band for the N-terminal antibody. The 70 kDa fragment (band c) was recognized by the N-terminal antibody (J2-1-50) and the J2-431-680 antibody, but not by the J2-565-580 antibody suggesting the removal of a C-terminal fragment due to cleavage somewhere before amino acid 565. The 28 kDa fragment (band d) was recognized by J2-431-680 and J2-565-580, but not the N-terminal antibody suggesting that it is a C-terminal

fragment with a cleavage somewhere before the S565 site. Band d may be generated by the same cleavage that generated the 70 kDa (band c) N-terminal fragment. We conclude that a large decrease in *Speg* allows *Jph2* to be calpain cleaved in skeletal muscle at sites in both the N- and C-terminal regions of *Jph2*. Surprisingly, despite a decrease in full-length *Jph2* in the skeletal muscle of HA-Speg mice, the fragments that increase in *Speg*-KO mice show small decreases in HA-Speg mice. This is likely to reflect different mechanisms of *Jph2* degradation in the two mice but suggests that *Jph2* fragmentation alone cannot explain the difference in skeletal muscle phenotypes in the two *Speg*-deficient mice. The N-terminal *Jph2* fragment (band c) may function as transcriptional regulators^{48–50}, was only in the *Speg*-KO skeletal muscle. Hence, the accumulation of a *Jph2*



N-terminal fragment is another factor that could contribute to differences in the phenotype of the Speg-KO and HA-Speg mice.

We also examined the Jph2 fragmentation patterns in the hearts of HA-Speg (Fig. 4f, g) and Speg-KO (Fig. 4h, i) mice. We did not detect the C-terminal 28-kDa fragment in the heart, possibly indicating that it is rapidly proteolyzed to smaller

fragments in the heart. Similar to skeletal muscle, the 91-kDa and 70-kDa fragments increased in the hearts of Speg-KO mice compared to controls and showed small decreases in the hearts of HA-Speg mice. The 70-kDa fragment is likely to be the N-terminal fragment identified to function as a transcription factor^{48–50}.

Fig. 3 Effects of Speg deficiencies on T-tubule structure and SR Ca²⁺ leak (sparks). FDB fibers were isolated from male mice as described in Methods. We used dual imaging of t-tubules (FM4-64) and Ca²⁺ (Fluo-4) to find areas of T-tubule disruption and SR Ca²⁺ leak. **a, b** T-tubule organization (raw and skeletonized) and spark localization (red squares) in FDB fibers from control (**a**) and HA-Speg (**b**) mice. **c** Spontaneous Ca²⁺ spark frequency in control ($N_{\text{fibers}}=21$, $N_{\text{animals}}=5$) and HA-Speg fibers ($N_{\text{fibers}}=28$, $N_{\text{animals}}=6$). **d** Analysis of T-tubule organization in control and HA-Speg fibers. **e, f** T-tubule organization (raw and skeletonized) and spark localization (red squares) in FDB fibers from control (**e**) and Speg-KO (**f**) mice. **g** Spontaneous Ca²⁺ spark frequency in control ($N_{\text{fibers}}=20$, $N_{\text{animals}}=5$) and Speg-KO fibers ($N_{\text{fibers}}=15$, $N_{\text{animals}}=3$). **h** Analysis of T-tubule organization in control and Speg-KO fibers. TE is the density of transverse elements; LE is the density of longitudinal elements. Regularity is the organization or spacing and is the magnitude of the major frequency derived from the FFT of the image. TTI is the t-tubule integrity, which considers both the regularity and density of the t-tubules. Data are plotted as the mean \pm SD, *** $P < 0.001$, ** $P < 0.01$, and * $P < 0.05$.

Using a Jph1 antibody to a C-terminal region (J1-554-572), we detected 57 kDa, 19 kDa, and 18 kDa fragments in both the TAs of WT and Speg-KOs, but none of the fragments increased in the Speg-KOs (Supplementary Fig. 4a, b), and this was not further investigated. For comparison, the Jph1 blots in the TA of HA-Speg mice are shown in Supplementary Fig. 4c, d.

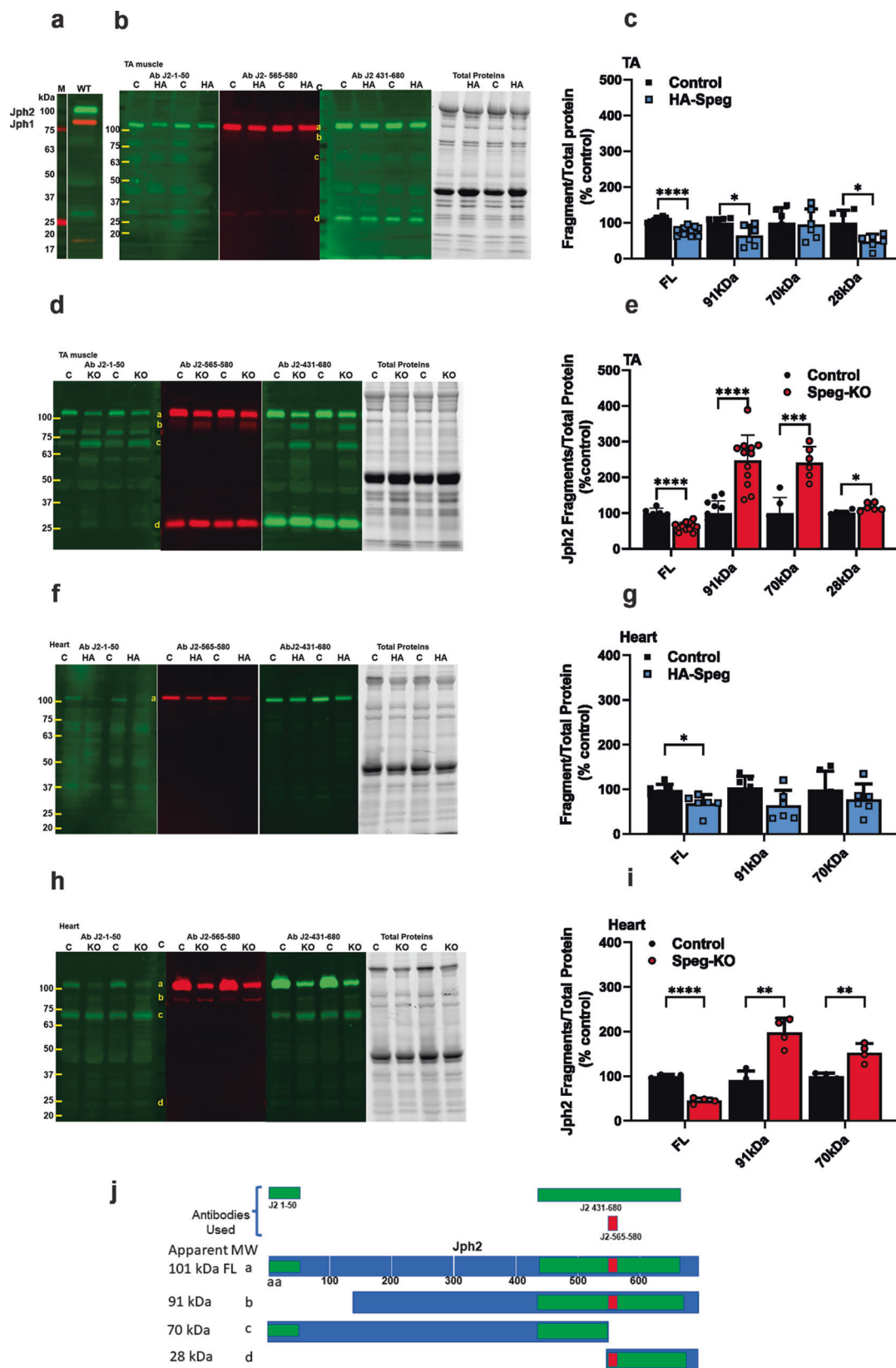
HA-Speg-binding proteins in triads. Despite the decrease in HA-Speg β levels in the skeletal muscle of the homozygous HA-Speg mice, the amount of remaining HA-Speg β was adequate to immunoprecipitate HA-Speg β binding proteins in both tissues. Nonspecific interactions were defined with HA antibody pull-downs from the muscle of WT mice. The data for this IP and all of the other IPs described below are presented in Supplementary Data 1, with different tabs for each IP (SD1-12). Proteomic data obtained from immunoprecipitations (IPs) with HA antibody from gastrocnemius muscles of HA-Speg and WT (nonspecific, ns) mice were analyzed by first removing all proteins that did not show >10 \times -fold purification (a minimal requirement for immune precipitation), and then we used a Holm-Sidaks multiple comparison test and/or false discovery rate (FDR)⁶⁶. A plot of false discovery rate is shown in Fig. 5a. The major cytosolic and ER/SR proteins in the HA-Speg pulldown were Speg, Esd (Esterase D, a serine hydrolase), Fsd2 (FN3/SPRY domain protein or minispryn), Cmya5 (Cardiomyopathy-Associated 5 protein or myospryn), Jph2 and Jph1. We do not consistently detect Serca, Dnm2, Mtm1, or desmin as specific in the HA-Speg IPs. We hypothesize that this could be due to: (1) HA-tag interference with these interactions, (2) low-affinity interactions and these proteins are lost during the washes, (3) differences in HA-Speg turnover in different cellular compartments compared to triads, leading to an enrichment of triadic proteins in the HA-Speg IPs and/or, (4) these previously identified Speg-binding proteins are binding exclusively to Speg.

Cmya5 is critical for the formation of cardiac dyads¹⁵ and interacts with Speg and RyR2¹⁵. Since Fsd2 and Esd have not been previously shown to be Speg-binding proteins, we used antibodies to these proteins and western blotting of the immunoprecipitates to confirm the presence of Speg in the IPs (Supplementary Fig. 5a, b). We found Esd and Speg specifically in the Fsd2 IPs and Fsd2 and Speg specifically in the Esd IPs, suggesting that these two proteins form a complex with Speg. To confirm these interactions, we immunoprecipitated Fsd2 and evaluated the immunoprecipitated proteins by mass spectrometry. A heatmap of the mass spec values (iBaq) for specific proteins (20 \times over IgG and $P < 0.01$) is shown in Fig. 5b. Also shown in this panel are the effects of Speg deficiency (Speg-KO). Note that Speg deficiency decreases the recovery of Fsd2 in the IP suggesting that, in this analysis, the effects of Speg could, at least partially, reflect the decrease in Fsd2. However, this is also a second measure of specificity. These data (ECC proteins indicated by red arrows) demonstrate that: (a) the major Fsd2 binding proteins are Tfg (Trafficking From ER To Golgi Regulator), Esd, Speg and Cmya5, (b) RyR1, Jph2, and Jph1 are also found in the

Fsd2 IP, and (c) Esd, Fsd2, Speg, Cmya5, RyR1, Jph2, and Jph1 are all significantly decreased in the Fsd2 IP from Speg-KO mice. To account for the loss in Fsd2 and the parallel loss in binding proteins, we normalized each proteins to the amount of Fsd2 in the IP and compared the Speg-KO samples to their controls (Fig. 5c). While Esd did not significantly decrease (suggesting it directly binds to Fsd2), Speg, Cmya5, RyR1, Jph1 and jph2 were effectively removed from the IP by the Speg deficiency. To determine if the decreased Fsd2 in the Fsd2 IP from the muscle of Speg-KO is due to decrease Fsd2 protein levels, we performed western blots for Fsd2 and Esd in TA homogenates from the controls and Speg-KO mice (Fig. 5d, e). Both Fsd2 and Esd protein levels were decreased in muscle homogenates from Speg-KO (Fig. 5d) and HA-Speg mice (Fig. 5e). Tfg was not altered by Speg deficiency but its presence in the Fsd2 IP may reflect a role of Fsd2 in vesicular trafficking, a possibility that requires further study.

The presence of Esd, Fsd2, and Cmya5 in the HA-Speg IP could reflect Speg interactions outside of triads/dyads. To address this, we used a BioID approach⁶⁷ to identify triadic proteins close to the immunophilin Fkbp12 binding site on RyR1. Fkbp12 binds with high affinity and specificity to RyR1 to stabilize the closed state of channel⁶⁸. Immunophilins, such as Fkbp12 and Fkbp12.6, are often used to purify RyRs for high-resolution cryoelectron microscopy (cryoEM) because of their high affinity and specificity for these channels⁶⁹⁻⁷¹. A construct to express Fkbp12-BirA (a biotinylating enzyme) was packaged into an AAV virus and injected into the gastrocnemius muscle of Fkbp12-deficient mice³¹ (MCK-Cre⁺Fkbp12^{fl/fl}). A construct to express GFP-BirA in AAV was used as a control and injected into the contralateral leg. Mice ($n=5$) were injected with biotin for 2 consecutive days prior to euthanasia at 3 weeks after the initial BirA virus injection, and the gastrocnemius muscle was isolated and homogenized. Biotinylated proteins were purified by streptavidin beads and identified by mass spectrometry. The specific biotinylated proteins were identified either as having a 10 \times fold purification over GFP-BirA and $P < 0.01$ or using false discovery rate, as shown in Fig. 5f. Near neighbors of FKBP12 in the triad included RyR1, Speg, Jph1, Jph2, Esd, Fsd2 and Cmya5. We also detected Ppp1r9b (Protein Phosphatase 1 Regulatory Subunit 9B) and Prpf4b (Pre-mRNA Processing Factor 4B, which is also a serine/threonine kinase). Ppp1r9b has been previously shown to bind to RyR2⁷². The significance, if any, of the interaction of Fkbp12 with Prpf4b remains to be determined. The biotinylation of Esd, Fsd2, and Cmya5 again suggests that these proteins are near the ECC apparatus in the triads. We did not detect specific labeling of triadin, calmodulin, PKA, or any of the subunits of Ca_v1.1, suggesting that these triadic proteins are not as close to the Fkbp12 binding site on RyR1 as the proteins in Fig. 5f.

RyR1- and Jph2-binding proteins from skeletal muscle from control, Speg KO, and HA-Speg mice. Since RyRs and Jph2 are likely interacting partners of Speg^{11,12,39}, we immunoprecipitated



RyR1 and Jph2 from skeletal muscle (gastrocnemius) of *Spieg^{fl/fl}* (control) and *Spieg*-KO mice to identify their binding proteins. In the proteomic experiments in Figs. 5 and 6, male mice were used to limit the number of mice since *Spieg* deficiency had similar effects in male and female mice in skeletal muscle and heart. Both RyR1 and Jph2 IPs were performed in 2 or more independent

experiments, and each experiment used 1–3 control and 1–3 *Spieg*-KO mice (*n* numbers for each experiment are provided in figure legends). Proteins in the IPs were identified by mass spectrometry. Datasets from each type of IP were pooled, and specific interacting proteins were identified by a 20X (RyR1) or 100x (Jph2) purification over IgG controls and a *P* < 0.01.

Fig. 4 Effect of Spieg deficiency on Jph fragmentation. **a** Western blot for Jph2 and Jph1 in the TA of WT mice. Red Jph1. Green Jph2. **b** Western blot for Jph2 fragments in the TA of control and HA-Speg mice stained with three different antibodies. The antibodies used in the blots are indicated in panel j (see Supplementary Table 3). The far-right panel in (**b, d, f, h**) is the total protein. **c** Analyses of fragments in TA of control and HA-Speg mice ($n = 6-13$). **d** Western blot for Jph2 fragments in the TA of Speg-KO and control mice. **e** Analysis of Jph2 fragments in TA control and Speg-KO mice ($n = 6-13$). **f** Western blot for Jph2 fragments in hearts of control and HA-Speg mice. **g** Analyses of fragments in control and HA-Speg hearts ($n = 6$). **h** Western blot for Jph2 fragments in control and Speg-KO hearts. **i** Analysis of Jph2 fragments in hearts of control and Speg-KO mice ($n = 4$). **j** Diagram of antibody binding sites and possible calpain-mediated cleavage sites. The tissues used in this experiment were all from male mice are FL- full-length Jph2, **b**—91 kDa, **c**—70 kDa, **d**—28 kDa. Data are plotted as the mean \pm SD. **** $P < 0.0001$, *** $P < 0.001$, ** $P < 0.01$, and * $P < 0.05$.

To compare proteins in the IPs of controls to those in the Speg-KO, all samples were normalized to the amount of Jph2 or RyR1 in the IP and batch-corrected (compared to control IPs for that specific experiment) to assess the effects of the Speg deficiency.

We found 21 proteins in the RyR1 IP that met the criteria of specific ($P < 0.01$, 20 \times enrichment over control IgG) in the immunoprecipitate. A heatmap of the “specific” proteins is shown in Fig. 5g. The red arrows indicate the proteins that are different in the IPs from Speg-KO mice. Many of the specific proteins are known RyR1 binding proteins, including Fkbp12, Casq1, Speg, Jph1, Jph2, Triadin, and CaMKII α and γ . Among the other proteins in the RyR1 IP, we find both Esd and Cmya5. Fsd2 is also present but is more variable than Esd and Cmya5 and does not reach a $P < 0.01$. Hence, at least two of the proteins identified in Fig. 5a, f are also in RyR1 IPs, again supporting the hypothesis that these proteins are triadic proteins. The significance (if any) of the presence of other proteins shown in the heatmap in Fig. 5g in the RyR1 IP is not yet known. RyR3 was also found in the RyR1 IP and is recognized by the same antibody as RyR1. We normalized each sample to the amount of RyR2 in that sample and then normalized to the mean of the control for that specific experiment. Specific proteins and proteins that are significantly different in the RyR1 IPs from Speg-KO mice are plotted in Fig. 5h. We found reductions ($P < 0.01$) in Casq1, Speg, obscurin (Obscn), Jph2, Jph1 and Cmya5 in the IPs from Speg-KO mice. For comparison, the ECC proteins reduced in the RyR1 IPs in the muscle of HA-Speg mice are shown in Fig. 5i. These data suggest that Speg interacts with RyR1 and/or an RyR1 binding protein and a major decrease in Speg causes dissociation of Casq1, Jph1 and 2, obscurin, Esd, and Cmya5 from RyR1. A curious finding in the RyR1 IPs was the presence of obscurin, a muscle giant protein that, like Speg, is a dual kinase of the MLCK family. We did not detect obscurin in either the HA-Speg IP (Fig. 5a) or the Fkbp12 BioID (Fig. 5f) experiment. While it is possible that the Speg antibody has affinity for obscurin, this would not explain the decrease in obscurin in the Speg-deficient mice. Obscurin links the sarcomere with the SR and interacts with titin and myomesin⁷³. The deficiency in obscurin could contribute to the phenotype of Speg-KO mice, but mice deficient in obscurin display only a mild myopathy with centralized nuclei⁷⁴.

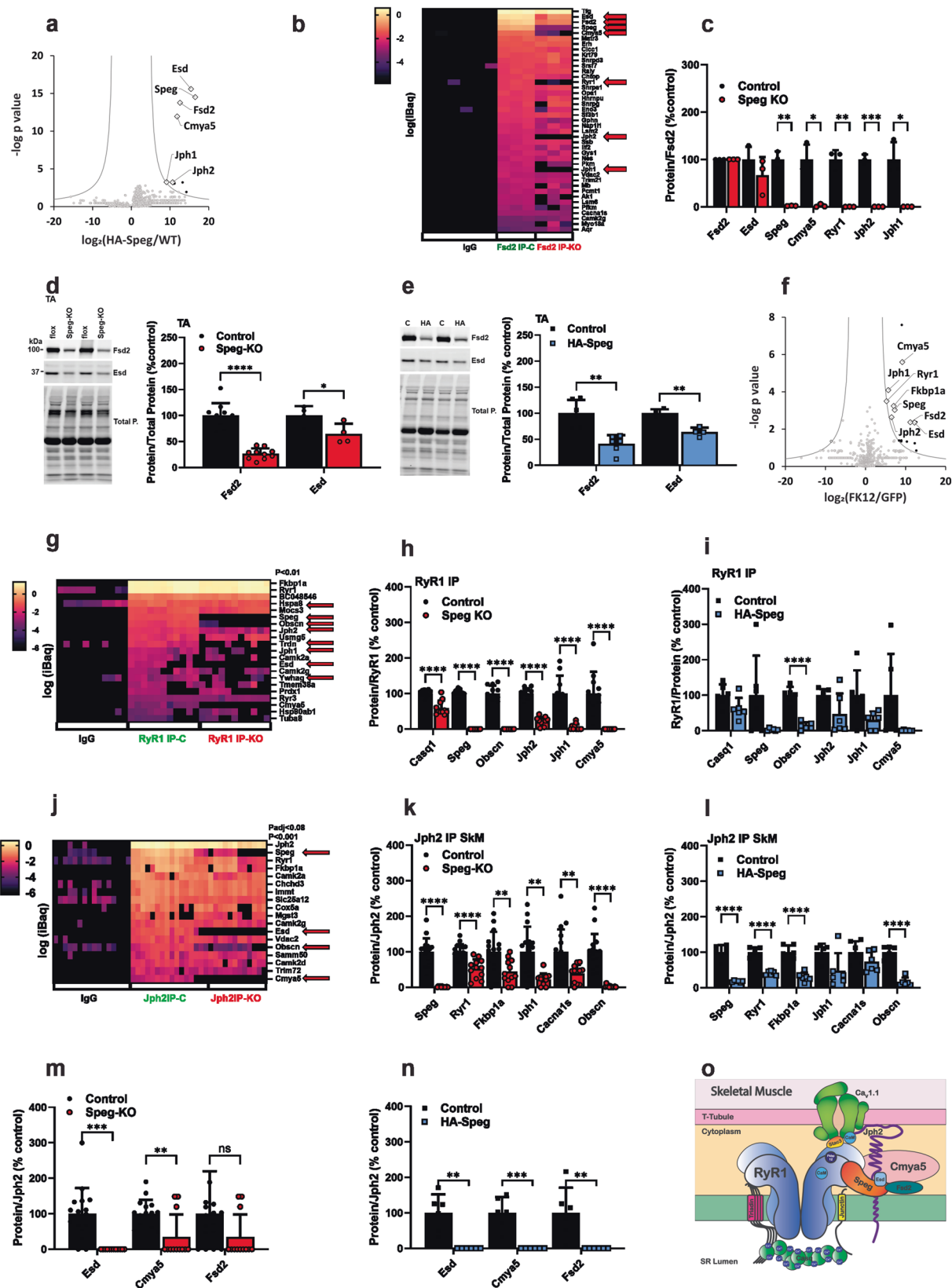
We immunoprecipitated Jph2 from the gastrocnemius muscles of control and Speg-KO mice. A heatmap showing “specific proteins” and proteins reduced in amount in the IPs by Speg deficiency is shown in Fig. 5j. The red arrows show proteins that are significantly different in the JPH2 IPs from Speg-KO mice and include Speg, Esd, Obscn. Specific proteins ($P < 0.01$, >100 purification over ns) included Jph2, Speg, RyR1, Asph (junctin), CaMKII (α , γ and δ), Esd, Cmya5, and Obscn. The immunoprecipitates of Jph2 from skeletal muscle had multiple ribosomal proteins that were removed for presentation purposes. We also performed a targeted comparison of ECC proteins in IPs from both Speg-KO (Fig. 5k) and HA-Speg (Fig. 5l) mice using the normalized and batch-corrected values (calculated as % control for each independent IP). The proteins in the control Jph2 IP were compared to those in Speg-KO IPs. As can be seen in

Fig. 5k, l, Speg deficiency in both mouse models decreased Speg, Fkbp12, RyR1, and Obscn in the Jph2 IPs. Cacna1s was significantly decreased in the Speg-KO but did not reach significance in HA-Speg IPs. The extent of reductions in Casq1, Speg and Obscn were greater in Speg-KO mice than in HA-Speg mice. We also compared the levels of Esd, Cmya5 and Fsd2 in the Jph2 IPs from Speg-KO (Fig. 5m) and HA-Speg (Fig. 5n) mice and found that the levels of these proteins were dramatically reduced in both models of Speg deficiency. A summary of the interactions of Speg and the identified Speg-binding proteins is shown in the model in Fig. 5o.

Speg, RyR2, and Jph2-binding proteins in cardiac muscle. The major Speg-binding proteins from the HA-Speg IPs from the heart were Speg, RyR2, Esd, Jph2, Cmya5 and Fsd2 (Fig. 6a). Cmya5 was previously identified as an RyR2 binding protein⁷⁵. Hence, in addition to confirming Jph2 and RyRs as Speg-binding proteins, we identified 3 Speg-interacting proteins, Esd (esterase D), Fsd2, and Cmya5, in both skeletal and cardiac muscle. Similar to the situation in skeletal muscle, Speg deficiency in hearts of both Speg-KO (Fig. 6b) and HA-Speg (Fig. 6c) mice led to decreases in Esd and Fsd2 in cardiac muscle homogenates. The extent of these decreases was similar in the two mouse models.

We performed RyR2 IPs from hearts of control (*Speg^{fl/fl}*) and Speg-KO mice. A heatmap for the specific proteins in the RyR2 IP from control and Speg-KO hearts is shown in Fig. 6d. The red arrow represents the proteins that are significantly different in the RyR2 IP from hearts of Speg-KO mice and include RyR2, Speg, Jph2 and Fsd2. We found 11 “specific” proteins in the RyR2 IP, including RyR2, phospholamban, BC048546 (Alpha-2-Macroglobulin-like protein, a protease inhibitor), Speg, Jph2, Esd, CaMKII δ , Ppapdc3 (an inactive sphingosine-1-phosphate phosphatase), Cmya5, Nfs1 (cysteine desulfurase) and Fsd2. We normalized each protein in the IP to the amount of RyR2 in the IP and then batch-corrected for each of the three independent experiments. Five proteins in the RyR2 IP from controls were significantly different in the IPs from hearts of Speg-KO (Fig. 6e), including Speg, Jph2, Esd, Cmya5, and Fsd2. Immunoprecipitations of RyR2 from the heart of HA-Speg mice were similar to those in the Speg-KO (Fig. 6f). Speg, Jph2, Esd, Cmya5 and Fsd2 were all reduced by Speg deficiency. BC048536 was reduced in the Speg-KO but was not reproducible in the HA-Speg.

We immunoprecipitated Jph2 from the hearts of controls, Speg-KO mice and HA-Speg mice. A heatmap of the values of a subset of proteins designated as specific is shown in Fig. 6g. The red arrows show values that are significantly different in the Speg-KO heart. Twenty-one proteins (ribosomal proteins removed) were identified as “specific” ($P < 0.01$ and 100 \times purification over IgG controls). We compared known ECC proteins in the IPs of the Speg-KO (Fig. 6h) and HA-Speg (Fig. 6i). Speg, RyR2, Casq2, Asph, and Trdn were all decreased in the Jph2 IPs from Speg-KO mice and Cacna1c was increased. Similar trends were seen in HA-Speg mice, but the extent of the decrease was less (Fig. 6i). Cacna1c was increased in the Jph2 IPs from HA-Speg mice. This is a major



difference from skeletal muscle, where the interaction of Jph2 with the voltage-dependent Ca^{2+} channel is decreased rather than increased by Speg deficiency. We also evaluated the levels of the three identified proteins and demonstrated that Esd, Cmya5 and Fsd2 were essentially absent in the Jph2 IPs from the hearts of both Speg-KO (Fig. 6j) and HA-Speg (Fig. 6k) mice. Since junctin binds

Casq, loss of these two proteins from the ECC complex in dyads may contribute to the more severe phenotype in Speg-KO mice. Immunoprecipitations of RyR2 and Jph2 from hearts of control and Speg-deficient mice suggest that the absence of Speg decreases the interactions among dyadic proteins and, similar to the situation in skeletal muscle, totally removes Esd, Cmya5, and Fsd2 from the

Fig. 5 **Speg-binding proteins and effects of Speg deficiency in skeletal muscle.** **a** Proteins immunoprecipitated from the gastrocnemius muscle of HA-Speg mice using antibodies against the HA-tag and identified by mass spectrometry ($n = 6$ for both the HA-IP from WT mice (nonspecific, ns) and the IP from HA-Speg mice). **b** Heatmap of immunoprecipitation of Fsd2 from Control and Speg-KO mice. ($n = 3$ for each). Also shown are IgG controls for nonspecific binding. **c** Analysis of the effects of Speg deficiency on Fsd2 binding proteins. **d** Effects of Speg deficiency on the levels of Fsd2 ($n = 10$) and Esd ($n = 4$) in homogenates from TA muscle of Speg-KO mice. A representative western blot is shown on the left. **e** Effects of Speg deficiency on the levels of Fsd2 ($n = 6$) and Esd ($n = 4$) in homogenates from TA muscle of HA-Speg mice. A representative western blot is shown on the left. **f** Proteins biotinylated by FKBP12-BirA compared to GFP-BirA. Proteins were purified with streptavidin beads and identified by mass spectrometry ($n = 5$ for each). **g** Heatmap of specific proteins in the RyR1 IP from the gastrocnemius muscle of control and Speg-KO mice ($n = 11$ for each). Nonspecific is shown as IgG. **h** RyR1 binding proteins in gastrocnemius muscle that are reduced in the RyR1 IP from Speg-KO mice ($n = 11$ for each). **i** RyR1 binding proteins in gastrocnemius muscle that are reduced in the RyR1 IP from HA-Speg mice ($n = 6$ for each). **j** Heatmap of specific proteins in the Jph2 IP from the gastrocnemius muscle of control and Speg-KO mice ($n = 14$ for control, $n = 12$ for Speg-KO). Also shown are IgG controls. **k** ECC proteins reduced in the Jph2 IP from muscle of Speg-KO mice. **l** ECC proteins reduced in the Jph2 IP from the muscle of HA-Speg mice ($n = 6-7$). **m** Effect of Speg deficiency on the relative amounts of Esd, Cmya5 and Fsd2 in the Jph2 IP from Speg-KO mice. **n** Effect of Speg deficiency on the relative amounts of Esd, Cmya5 and Fsd2 in the Jph2 IP from HA-Speg mice. **o** Model summarizing the findings from the proteomic studies in skeletal muscle. Data are plotted as the mean \pm SD. **** $P < 0.0001$, *** $P < 0.001$, ** $P < 0.01$, and * $P < 0.05$.

dyadic complexes. A model of the dyads' protein interactions is shown in Fig. 6l.

Discussion

Excitation-contraction coupling is conducted by a highly complex assembly of conformationally coupled proteins localized to triads and dyads. The interactions of Speg and Jph2 and the consequences of Speg deficiency have been studied in cardiac^{5,11,12}, and skeletal muscle^{10,14,15,39} but many questions especially about the targets of Speg both with respect to binding partners and phosphorylation targets in the dyads and triads remain to be fully defined. To elucidate the role of Speg in triad and dyad function, we created a mouse model of Speg deficiency (HA-Speg mice) that serves dual purposes of facilitating the identification of Speg-binding proteins and serving as a model of Speg deficiency with Speg β and Spega expression decreased by ~95% and 50%, respectively, in skeletal muscle of homozygous HA-Speg mice (Fig. 1a). In hearts of HA-Speg mice, Speg β and Spega levels were reduced by ~80% and 40%, respectively (Fig. 1c). The decrease in Speg β protein levels in these mice likely reflects an effect of the inserted tag on both transcription (Speg β mRNA decreased by ~50%) and increased turnover of the Speg β protein. The 3XHA-Tag is known to alter protein stability⁵⁵. Spega is produced by transcription initiation at a second promoter site within the *Speg* gene and differs from Speg β only in the N-terminus where it is missing 854 amino acids. Spega is, therefore, not labeled by the HA-tag. This raises the question of why there is a decrease in Spega in HA-Speg mice. We detect no differences in the mRNA for Spega, suggesting that the decrease is more likely due to increased protein turnover. We find that Spega forms heterooligomers with Speg β , suggesting that complexed Spega may be targeted for degradation. We propose that the HA-Speg mice are a mouse model of Speg β deficiency while sparing Spega to some degree, perhaps serving a mouse model of the relatively mild myopathy in humans associated with decreased Speg β with sparing of Spega⁷. In contrast, MCK-Cre⁺Speg^{fl/fl} mice¹¹ (which we designate as Speg-KO mice) display a >95% decrease in both Speg β and Spega in both skeletal muscle (Fig. 1b) and heart (Fig. 1d) and display a life-threatening myopathy where both skeletal and cardiac muscle are severely affected.

In comparing HA-Speg and Speg-KO mice, we found intriguing similarities and differences that shed light on the drivers of the more severe phenotype (weakness and atrophy in skeletal muscle and dilated cardiomyopathy) of Speg-KO mice. All muscles evaluated (EDL, soleus, and diaphragm in male and female mice) from Speg-KO mice displayed major reductions in ability to generate force and rightward shifts in the force-frequency curves. The most affected muscle in Speg-KO mice was

the EDL. All three fiber types (IIa, IIx, and IIb) in the EDL show large decreases in CSA (Fig. 2h, l) with fiber-type distribution changes (Fig. 2l). In contrast, HA-Speg mice showed almost total sparing of the EDL muscle with respect to force generation, CSA, and changes in fiber-type distribution. The soleus and diaphragm muscles of HA-Speg mice have a decreased ability to generate force. In addition, the HA-Speg mice do not develop a dilated cardiomyopathy. These findings suggest that Spega in HA-Speg mice can at least partially compensate for the loss of Speg β in both skeletal and cardiac muscle and can completely rescue the EDL (the most affected muscle evaluated in the Speg-KO), suggesting that Spega is critical in fast twitch muscles like the EDL.

In addition to reduced force generation, the skeletal muscle of Speg-KO mice displayed abnormal triads and altered Ca²⁺ handling and ECC³⁹. Speg deficiency in cardiac tissue leads to heart failure (HF) with increased SR Ca²⁺ spark frequency and disruption of the t-tubules¹². Because of the association of Speg deficiency with altered Ca²⁺ handling and t-tubule structure, we compared t-tubule structure and the frequency of spontaneous Ca²⁺ sparks in FDB fibers from control and Speg-KO mice and from control and HA-Speg mice (Fig. 3). In HA-Speg mice, we found small but significant increase in Ca²⁺ sparks and we found small areas of t-tubule disruption. Intriguingly, the Ca²⁺ sparks appeared to localize to these areas of t-tubule disruption (Fig. 3b). In contrast, the FDB fibers of Speg-KO mice displayed major areas of t-tubule disruption and a marked increase in spontaneous Ca²⁺ sparks. Again, the Ca²⁺ sparks in the fibers from Speg-KO mice primarily localize in areas of t-tubule disruption. The differences in the Ca²⁺ spark frequency and t-tubule disruption correlate with the relative severity of the muscle dysfunction in the HA-Speg versus Speg-KO mice. Our data suggest that both t-tubule disruption and Ca²⁺ leak are intricately linked phenomena associated with Speg deficiency and contribute to an amplifying feed-forward mechanism that leads to loss of muscle function. It is highly likely that both increased Ca²⁺ sparks and t-tubule disruption must occur to cause the severe cardiac and skeletal muscle functional losses in the Speg-KO mice. A contribution of decreased muscle satellite cells in the Speg-KO phenotype⁴⁰, especially the extensive EDL atrophy, is likely but requires further study.

Cardiac stress correlates with decreased Jph2⁵⁸⁻⁶⁰. In response to elevation in cytosolic Ca²⁺ levels, Jph2 undergoes calpain-mediated cleavage into fragments^{49,50,61,62}, and the N-terminal fragment moves to the nucleus to function as a stress-activated transcriptional repressor⁵⁰. A C-terminal Jph2 fragment also translocates into the nucleus, where it is believed to affect hypertrophic signaling⁴⁸. Calpain-mediated cleavage of Jph2 is a likely cause of t-tubule disruption^{23,45,50,51,61,65}. Junctophilins are

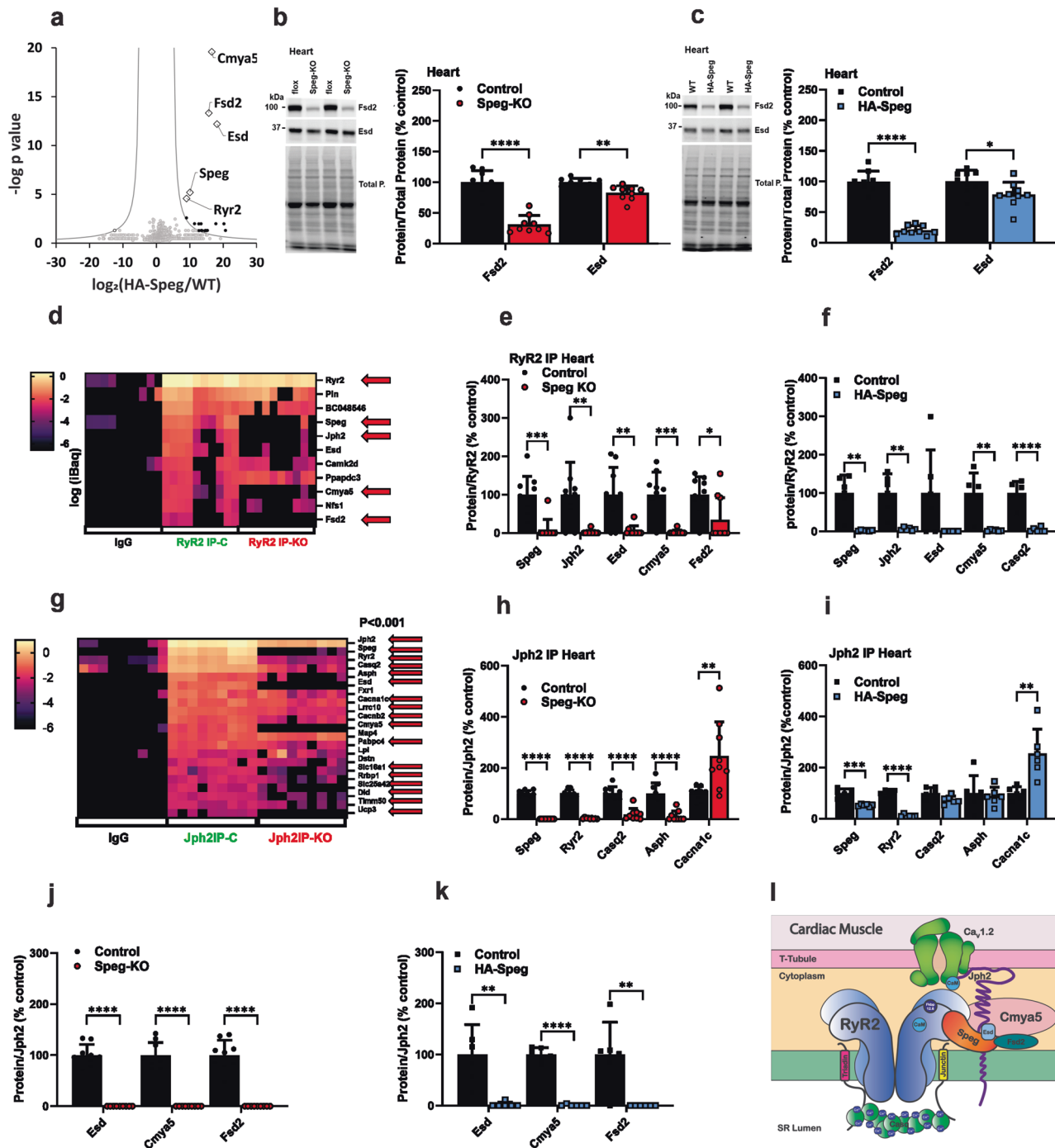


Fig. 6 Speg-binding proteins and effects of Speg deficiency in the heart. **a** Proteins immunoprecipitated from the hearts of HA-Speg mice using antibodies against the HA-tag and identified by mass spectrometry ($n = 6$ for each). **b** Effects of Speg deficiency on the levels of Fsd2 ($n = 8$ for each) and Esd ($n = 9$ for each) in homogenates from hearts of Speg-KO mice. A representative western blot is shown on the left. **c** Effects of Speg deficiency on the levels of Fsd2 and Esd in homogenates from hearts of HA-Speg mice ($n = 6$ for each). **d** Heatmap of specific RyR2 binding proteins from the hearts of control and Speg-KO mice ($n = 9$ for each). **e** Proteins that are significantly changed the cardiac RyR2 IP from controls compared Speg-KO mice. **f** Proteins that are significantly changed the cardiac RyR2 IP from controls compared HA-Speg mice ($n = 6$ for each). **g** Heatmap of specific Jph2-binding proteins from the hearts of control and Speg-KO mice ($n = 9$ for each). **h** Proteins that are significantly changed the cardiac Jph2 IPs from controls compared Speg-KO mice. **i** Proteins that are significantly changed the cardiac Jph2 IPs from controls compared HA-Speg mice ($n = 6$ for each). **j** Effect of Speg deficiency on the relative amounts of Esd, Cmya5 and Fsd2 in the cardiac Jph2 IP from Speg-KO mice. **k** Effect of Speg deficiency on the relative amounts of Esd, Cmya5, and Fsd2 in the cardiac Jph2 IP from HA-Speg mice. **l** Model summarizing the findings from the proteomic studies in cardiac muscle. Data are plotted as the mean \pm SD. **** $P < 0.0001$, *** $P < 0.001$, ** $P < 0.01$, and * $P < 0.05$.

required for maintenance of the structure of triads in skeletal muscle and dyads in cardiac muscle⁶³, but neither the N- nor C-terminal Jph2 fragments rescue ECC in Jph2-deficient cardiomyocytes⁶⁵, suggesting that the transmembrane domain at the C-terminus that anchors Jph2 to the SR membrane and the N-terminus that is involved with interactions with t-tubules are both required to prevent dyadic uncoupling and disruption of ECC. Both Spieg-KO and HA-Spieg mice displayed decreases in RyR1, Ca_v1.1α1 (Cacna1s), and Jph2 in skeletal muscle, with the decreases being greater in the Spieg-KO muscle. Neither RyR2 nor Ca_v1.2α1 (Cacna1c) were decreased in the Spieg-KO or HA-Spieg hearts. Jph2, however, was decreased in both the HA-Spieg and Spieg-KO hearts with the extent of the decrease greater in Spieg-KO mice. Hence, ECC proteins appear to be targeted for turnover in skeletal muscle but not in the heart by Spieg deficiency. We examined the Jph2 fragmentation patterns in skeletal and cardiac muscle of controls, Spieg-KO, and HA-Spieg mice and found that sites at both the N- and the C-terminus of Jph2 were more accessible to cleavage in both heart and skeletal muscle of Spieg-KO mice, but not HA-Spieg mice (Fig. 4). These studies suggest that Spiegα and Spiegβ normally protects Jph2 from calpain cleavage, but, in HA-Spieg mice, the presence of Spiegα alone can protect Jph2 from this cleavage.

The primary sequence of Spieg suggests that it interacts with other proteins and, also, as a dual kinase, phosphorylates multiple protein targets. Both RyRs¹¹ and Jph2¹² are phosphorylated by Spieg. Whether the functional consequences of Spieg deficiency in either skeletal muscle or heart arise from altered phosphorylation of Spieg targets and/or from alterations in Spieg interactions with other proteins is not yet known. The loss of phosphorylation of RyRs at the site of phosphorylation by Spieg could alter open probability directly and/or decrease RyRs interaction with a modulatory protein that controls its opening. In addition, it is possible that RyR2 phosphorylation itself affects the binding of various interacting proteins⁷⁶. Either mechanism could lead to SR Ca²⁺ leak. Loss of Jph2 phosphorylation by Spieg deficiency could alter its sensitivity to calpain cleavage and its ability to stabilize t-tubules. Alterations in Jph2 phosphorylation or its calpain cleavage could also alter its ability to interact with RyRs or voltage-dependent Ca²⁺ channels. These possibilities argue for the need for more information about Spieg interactions in both cardiac and skeletal muscle.

While HA-Spiegβ expression levels are greatly decreased in the muscle of HA-Spieg mice, HA-Spiegβ is expressed at adequate levels to purify and identify Spieg-binding proteins. To evaluate the effects of Spieg deficiency on protein-protein interactions within triads and dyads, we used HA-Spieg to immunoprecipitate Spieg-binding proteins from skeletal muscle and heart and found that Esd, Cmya5, Fsd2, Jph1, and Jph2 were associated with Spieg in skeletal muscle and Esd, Cmya5, Fsd2, Jph2, and RyR2 were associated with Spieg in cardiac muscle. We confirmed these interactions using Fsd2 immunoprecipitation in skeletal muscle and showed that RyR1, Cmya5, Jph2, and Jph1 interactions with Fsd2 require Spieg. We also showed that these proteins are localized to skeletal muscle triads using a BioID approach with Fkbp12-BirA. Finally, we immunoprecipitated RyR1 and Jph2 from homogenates of skeletal muscle and RyR2 and Jph2 from homogenates from the heart and showed that RyR1, RyR2 and Jph2 (both cardiac and skeletal muscle) interact with Cmya5, Fsd2 and Esd in a Spieg-dependent manner. Determination of whether these proteins interact with low affinity with all triads/dyads or with high affinity to a subset of triads/dyads will require additional studies with different approaches, such as near-neighbor crosslinking and localization studies.

Another particularly important aspect of our studies is that Spieg regulates the interactions of known components of triads

and dyads. Spieg deficiency decreases the interaction between Jph2 with RyR1 in skeletal muscle and between Jph2 and RyR2 in cardiac muscle, as shown in both RyR and Jph2 IPs. In skeletal muscle Jph2 IPs, Spieg deficiency decreases the Jph2 interaction with Ca_v1.1α1s but in cardiac tissue Spieg deficiency increases its interaction with Ca_v1.2α1c. This difference may reflect differences in the rate at which the N-terminal Jph2 fragment dissociates from the voltage-dependent Ca²⁺ channels to move it to the nucleus in the two tissues.

The presence of obscurin in the RyR1 and Jph2 IPs was unexpected, as was its loss in the IPs from Spieg-KO mice. Obscurin deficiency impairs skeletal muscle Ca²⁺ handling⁷⁷ and, hence, the loss of obscurin in the RyR and Jph2 IPs in Spieg-KO mice could contribute to the phenotype. This finding raises the possibility that obscurin alters Ca²⁺ handling in skeletal muscle via direct interactions within the triad. Unlike Cmya5, Esd, Fsd2, Jph1, Jph2, and RyR1, obscurin is not found in the HA-Spieg IPs from skeletal muscle, suggesting that its interaction is not directly with Spieg but its presence in the triads may require an action (e.g., phosphorylation) or interaction of Spieg.

Fsd2 (also called minispryn) and Cmya5 (also called myospryn) are paralogs that have previously been shown to interact with RyR2⁷⁵. Immunoprecipitation of Fsd2 led to coimmunoprecipitation of ECC proteins, Cmya5 and Esd. Only the interaction of Esd with Fsd2 was not dependent on the presence of Spieg, suggesting that Esd and Fsd2 form a complex. Cmya5 promotes RyR2 clustering in heterologous cells⁷⁵, plays a critical role in maintaining cardiac dyad architecture and positioning⁴³ and its ablation causes dyad disruption and SR Ca²⁺ leak, leading to cardiac dysfunction⁴³. Cmya5 is also considered to be a biomarker for several striated muscle diseases^{78,79}. The third Spieg-dependent component of the ECC complex is Esterase D, a widely expressed esterase with both carboxylesterase and thioesterase activity that plays critical roles in drug metabolism and suppression of cancer growth⁸⁰. Our data strongly support a role for Spieg bringing Esd, Fsd2, and Cmya5 to triads and dyads to stabilize these structures. One potential role for Spieg, Esd, Fsd2, and Cmya5 in skeletal and cardiac muscle is to drive or maintain clustering of RyRs to stabilize triads and dyads. Such a role is consistent with the loss of interactions among ECC proteins in the absence of Spieg.

A major question raised by our study is which of the differences between the HA-Spieg and Spieg-KO mice are the cause of the more severe phenotype of the Spieg-KO mice. Cmya5, Fsd2 and Esd are lost from the ECC proteins of both triads and dyads in both mouse models and, hence, this loss alone cannot account for the Spieg-KO phenotype. Since these same proteins are lost from triads and dyads in HA-Spieg mice, their presence in triads and dyads must be dependent on Spiegβ rather than Spiegα (spared in HA-Spieg mice). Spieg-KO mice have increased Ca²⁺ sparks, more t-tubule disruption, and display increased accumulation of calpain-mediated Jph2 fragments compared to HA-Spieg mice, suggesting that Spiegα may limit these events in the HA-Spieg mice. In an inducible cardiac-specific Spieg knockout mouse model, Ca²⁺ sparks were not detected until after heart failure¹², suggesting that Spieg deficiency does not necessarily directly lead to Ca²⁺ sparks. Instead, Quick et al.¹² suggested that acute loss of Spieg leads to decreased Jph2 phosphorylation and disruption of t-tubules.

Spiegβ interacts with Esd, Fsd2, and Cmya5 and localizes these proteins to triads and dyads. The HA-Spieg mice, while having a phenotype that is milder than the Spieg-KO, display decreases in force generation in the soleus and diaphragm with almost total sparing of the EDL, suggesting that the phenotype may manifest primarily in muscles that are constantly working. In this situation, the contributions of Cmya5, Esd, and Fsd2 to stabilization of the

triadic and dyadic ECC complex may play a more important role in muscle function. Our data suggest that, while t-tubule disruption may be a driver of the disease, the Speg-mediated mechanisms that drive t-tubule disruption are likely to be multifactorial and involve a series of closely coupled events including altered Jph2 phosphorylation¹², altered SERCA activity¹³, increased Ca²⁺ sparks, calpain-mediated cleavage of Jph2, and destabilization of interactions among the components of the triads and dyads due, at least partially, to the loss of Cmya5, Esd, and Fsd2.

Methods

Materials. All antibodies used are listed in Supplementary Table 3.

Mice. The floxed Speg (*Speg^{fl/fl}*) mice were obtained ES cell clone EPD0180_2_A07 obtained from the KOMP repository (www.komp.com) and generated by the Wellcome Trust Sanger Institute. HA-Speg mice were created in the Genetically Engineered Rodent Model (GERM) Core at BCM. All mouse experiments complied with relevant ethical regulations for animal tested and were performed under IACUC protocol AN-2656.

CRISPR-mediated knock-in allele design and reagent production for HA-Speg mice (Supplementary Fig. 1). To generate the *Speg-V5-3xHA* tag KI allele, a CRISPR-based targeting strategy was designed by the BCM Genetically Engineered Rodent Model Core (BCM GERM Core). The Core has experience in designing and producing mouse models^{81–84}. Single-guide RNAs (gRNAs) were selected using the Wellcome Trust Sanger Institute Genome Editing website. This gRNA targets a double-strand break proximal to the initial methionine within the coding sequence of Speg (<https://wge.stemcell.sanger.ac.uk/crispr/307086362>) and was synthesized by Synthego (Redwood City, CA). The gRNA chosen had no predicted off-target sites with less than 3-base mismatches in exons or on the same chromosome. To introduce the V5-3xHA sequence into the N-terminus of *Speg*, a donor DNA template was synthesized by IDT (Coralville, IA) as a megamer. Single-guide RNA (20 ng/μL), Megamer (30 ng/μL), and Cas9 mRNA (100 ng/μL; Thermo Fisher Scientific, Waltham, MA) were mixed in a final volume of 50 μL 1x Modified TE (RNase-free).

Microinjection of CRISPR/Cas9 reagents. C57BL/6J female mice, 24–32 days old, were injected with 5 IU/mouse of pregnant mare serum, followed 46.5 h later with 5 IU/mouse of human chorionic gonadotropin, and later mated to C57BL/6J males. Fertilized oocytes were collected at 0.5 dpc for microinjection. The BCM Genetically Engineered Mouse Core microinjected the sgRNA/donor/Cas9 mixture into the cytoplasm of at least 200 pronuclear stage zygotes. Injected zygotes were transferred into pseudo-pregnant ICR females on the afternoon of the injection, ~25–32 zygotes per recipient female.

Genotyping. Allele characterization was performed by standard PCR to identify founders with the inserted V5-3xHA tag, followed by Sanger sequencing. Three separate PCR reactions were performed, one reaction spanning the full insert (F 5'-CTCC ACTGCTCATTCGCAAC, R 5'-CATCCCGGAACCAGCTGAG, F + R = 472 bp WT allele, 628 bp targeted allele) and two reactions to cover from outside each homology arm to the middle of the inserted sequence (5' arm F: 5'-CTCCACTGCTCATTCGC AAC-3', 5' arm R: 5'-TAGCCCGCATAGTCAGGAAC-3', 314 bp targeted allele; 3' arm F: 5'-AGCCTATCCCTAACCCTCTCCT-3', 3' arm R: 5'-CTACTACCCGCAGCCTTACA-3', 356 bp). Mice with the appropriately sized band for the targeted allele and PCR

products for the two homology arm reactions were sequenced to verify the integrity of the targeted sequence. Targeted HA-Speg N0 founders were backcrossed with stock C57BL/6J animals to generate N1 pups. Heterozygous HA-Speg N1 mice had the same PCR assays performed, followed by sequence confirmation prior to establishing a colony from a limited number of N1 animals.

Echocardiography. Left ventricular function in mice was assessed by echocardiography using a VisualSonics Vevo F2 imaging system equipped with a frequency probe (40 MHz) in the BCM Mouse Metabolism & Phenotyping Core. After being anesthetized by 2% isoflurane mixed with 100% O₂, mice were placed on a heated pad where all four limbs were taped down onto surface electrodes to measure ECG. On the plate, anesthesia was maintained with 1.5% isoflurane. Body temperature was monitored using a rectal thermometer and kept between 36.5 °C and 37.5 °C. M-mode measurements were recorded at heart rates of 500 ± 50 bpm.

Gene expression analysis. Total RNA was extracted from mouse tissues using TRIzol reagent (Life Technologies) and purified using the RNeasy Fibrous Tissue Mini Kit (Qiagen). The purified RNA was reverse transcribed into cDNA using the SuperScript IV VILO Master Mix (Invitrogen). Gene expression assay was performed with the TaqMan Fast Advanced Master Mix (Applied Biosystems) using the following TaqMan probes: *Spegβ* (Mm00812485_m1), *Spegα* and *β* (Mm00812511_m1), *Apeg-1* and *Bpeg* (Mm00500180_m1). Using the qPCR BIO SyGreen Blue Mix Lo-ROX (PCR Biosystems), the following primers were used: *Spegα* F: 5'-TTCCTTCCCTGCACATTCC-3' and *Spegα* R: 5'-TCTCCTGGGTGCTGTCTC-3'.

Samples were run in technical triplicates on the ViiA 7 Real-Time PCR System (Applied Biosystems). Mean Ct values for each gene were normalized against house-keeping genes *β-actin* (Mm02619580_g1) or *Gapdh* F: 5'-AGGTCGGTGTGAACGG ATTTG-3' and R: 5'-TGTAGACCATGTAGTTGAGGTCA-3' to obtain ΔCt. ΔΔCt, which was calculated after normalizing to WT values, were then log₂-transformed to obtain fold change values.

Ex vivo force measurement. As described previously^{68,85}, intact muscles were dissected and placed in a dish with fresh Krebs-Ringer solution (137 mM NaCl, 5 mM KCl, 1 mM NaH₂PO₄, 24 mM NaHCO₃, 5 mM glucose, 2 mM CaCl₂ and 1 mM MgSO₄) bubbled with a 5/95% mixture of CO₂/O₂. Muscles were tied and suspended between a force transducer and glass stationary anchor to equilibrate in a 34 °C bath. To get the optimal muscle length, a series of electrical stimulations for single twitches (train rate: 1 tps, train duration: 200 ms/train, stimulation duration: 0.2 ms/pulse, voltage: 20 V, resistance: 25 Ω) were applied to the muscles. Muscles were then adjusted to the length that allowed them to generate the strongest isometric tension. Force measurements were acquired by applying 250 ms trains using the frequencies 1 Hz, 15 Hz, 30 Hz, 40 Hz, 60 Hz, 80 Hz, 160 Hz, and 300 Hz, separated by a 1–2-min rest time. Muscle stimulation was applied using platinum electrodes attached to a Grass S48 stimulator, and muscle contracture was recorded by Chart5 (version 5.2).

Sequential visualization of Ca²⁺ sparks and t-tubules in living fibers. As previously described⁸⁶, intact FDB muscles were dissected from mice and incubated in DMEM (Thermo Fisher Scientific) containing 0.1% penicillin-streptomycin (Thermo Fisher Scientific) and 0.4% collagenase A (Sigma) at 37 °C for 2.0 h. Following enzymatic digestion, isolated fibers were transferred to DMEM supplemented with 10% FBS and incubated in 5% CO₂ at 37 °C overnight. For measurement of spontaneous Ca²⁺ sparks,

isolated FDB myofibers were loaded with the Ca^{2+} -sensitive dye Fluo-4AM (5 μM ; Invitrogen) prepared in HEPES-Ringer solution (140 mM NaCl, 4.0 mM KCl, 1.0 mM MgSO_4 , 5.0 mM NaHCO_3 , 10.0 mM glucose, 10.0 mM HEPES, pH 7.3) for ~30 min at 37 °C and washed 3 times with dye-free HEPES-Ringer solution, followed by a rest period of 15 min to allow for dye de-esterification. T-tubules were visualized by incubating the fibers in the lipophilic styryl membrane marker FM 4-64 (6.5 mM, Thermo Fisher Scientific) for 10 min. High-resolution images were obtained on a Zeiss LSM 880 with a 40 \times NA1.2 water objective. The pixel dimensions were 0.06 \times 0.06 μm in the x - and y axes. Fluo-4 was excited at 488 nm, and the emission intensity was captured between 491 and 556 nm in confocal mode. A sequence of 30 XY images was collected over time, and the frequency of sparks was determined from the Fluo-4 channel using custom routines written in IDL as previously described⁸⁷. After Fluo-4 imaging, FM⁴-64 was excited at 561 nm, and emission intensity was measured with an LP 650 nm in Super-resolution Airyscan mode in the same z -plane. The x and y locations of the spark centers were mapped onto the t-tubule image, and 100 μm^2 regions of interest centered at the center of the spark were extracted for processing of the t-tubule structure using AutoTT⁸⁸. As control wild-type myofibers do not elicit Ca^{2+} sparks, we used the spark centers obtained from Speg-deficient myofibers imaged the same day to select t-tubule regions of interest in a nonbiased fashion.

Body composition. Mice were anesthetized with isoflurane and assessed using the dual-energy x-ray absorptiometry (DEXA) system (Faxitron, Tucson, AZ, USA).

Fiber typing and cross-sectional area. Soleus and EDL muscles were dissected, embedded in OCT compound (Tissue-Tek), and frozen in 2-methylbutane. Frozen muscles were cut into 10 μm sections and stored at -20 °C. Frozen sections were prepared for fiber typing and experiments, as previously described⁵⁶.

Immunoprecipitations. Gastrocnemius muscle and heart from HA-Speg, Speg-deficient, and control mice were homogenized in six to eight volumes of IP buffer (w/v) (50 mM Tris-HCl, pH 7.4, 170 mM NaCl, 1 mM EDTA, and 1% NP-40) containing protease and phosphatase inhibitors using a bead homogenizer (Precellys[®] tissue homogenizer). After centrifugation, the cleared supernatant was incubated with primary antibodies and nonimmunized IgG for 1 h (for RyR) to overnight (for Jph2 and HA-tag). After incubation with primary Ab, 40 μl of magnetic beads (Dynabeads[®] Protein G, Invitrogen) were added and incubated for 1 h at 4 °C. Magnetic beads were washed three times with IP buffer and twice with sterile PBS using a magnetic stand. Washed beads were trypsinized for mass spectrometry.

SDS-PAGE and western blot. Skeletal muscle and heart were snap-frozen in liquid nitrogen and stored at -80 °C until use. Skeletal muscle and heart were thawed and homogenized in RIPA buffer (150 mM NaCl, 1% NP-40, 0.5% sodium deoxycholate, 0.1% SDS, and 50 mM Tris-HCl, pH 8.0) supplemented with a protease and phosphatase inhibitor cocktail by using a bead homogenizer (Precellys 24 homogenizer, Bertin Instruments, Paris, France). Protein concentrations were determined using a BCA assay. Homogenates (60 μg) were separated by SDS-PAGE using the Bio-Rad Stain Free gel system to enable total protein visualization and quantitation. Proteins on PAGE gels were transferred to PVDF membranes (Immobilon-FL, EMD Millipore), blocked in EveryBlot blocking buffer (Bio-Rad), and incubated with primary antibodies overnight at 4 °C.

After washing in PBS containing 0.2% Tween-20 (PBST), membranes were incubated with fluorophore-tagged Starbright secondary antibodies (Bio-Rad) for 1 h at room temperature. After washing in PBST, blots were imaged on a Chemidoc MP system (Bio-Rad). Total protein using stain-free gels (Bio-Rad), after transfer of the proteins to the PVDF membrane (Immobilon[®]-FL, Millipore), the PVDF membrane was imaged by using a ChemiDoc[™] MP imaging system (Bio-Rad). All antibodies used are provided in Supplementary Table 3.

BioID constructs. All BioID constructs used here were based on pENTRY-EF1a (Invitrogen). The coding sequences of FKBP12 or GFP were fused with that of BirA*, followed by P2A-acGFP in pENTRY-EF1a. P2A-AcGFP was added to mark transfected cells (Supplementary Fig. 6A, B).

AAV production. AAV transgene plasmids (Supplementary Fig. 5) containing AAV2 inverted terminal repeats (ITRs) were constructed using gene synthesis and standard molecular biology techniques. Plasmid “1533_pAAV-CB-AcGFP-BirA-HA” expresses an *Aequorea coerulescens* GFP (AcGFP) with a Gly-Gly-Ser-Gly flexible linker fused to a C-terminal BirA* biotin ligase followed by an Ala and a Hemagglutinin (HA) epitope tag. The transgene cassette is driven by a chicken beta-actin promoter with a CMV enhancer element and includes a 3' woodchuck hepatitis virus posttranscriptional regulatory element (WPRE) and bovine growth hormone polyadenylation signal downstream. A plasmid in the identical configuration named “1529_pAAV-CB-FKBP12-BirA-HA” was generated to express the murine FKBP12-BirA-HA fusion protein. AAV vectors based on serotype 9 were generated by the triple transfection method of Xiao et al.⁸⁹ in HEK293T cells with minor modifications⁹⁰. AAV9 was purified by CsCl density gradient ultracentrifugation, dialyzed, concentrated in phosphate-buffered saline, aliquoted, and stored at -80 °C until use. Viral titers were determined by qPCR with SYBR green compared to a standard curve from tenfold serial dilutions of the respective transgene plasmid. Primers specific to the WPRE were used: AH_0104—5'-CATTGCCACCACCTGTCC-3'; AH_0105—5'-GACGTAGCAGAAGGACGTCC-3'.

Mass spectrometry. Immunoaffinity purification followed by nanoHPLC-MS/MS analysis was used for interactome as previously reported with minor modifications⁹¹. Briefly, the affinity-purified protein and interacting proteins are digested on beads using Trypsin/Lys-C enzyme, then the digested peptide is enriched and desalted by in-house STAGE tip⁹² column with 2 mg of C18 beads (3 μm , Dr. Maisch GmbH, Germany) and vacuum dried. Resuspended peptides were analyzed on an nLC 1000 coupled with an Orbitrap Fusion mass spectrometer (Thermo Scientific) with an ESI source. Data acquisition was performed in data-dependent analysis mode (DDA) for unbiased peptide detection. The obtained spectra were processed by the Proteome Discoverer 2.1 interface (PD 2.5, Thermo Fisher) with the Mascot algorithm (Mascot 2.1, Matrix Science). Assigned peptides were filtered with a 1% false discovery rate (FDR) using percolator validation based on the q -value. The calculated area under the curve of peptides was used to calculate the iBAQ for protein abundance using in-house software⁹³.

Statistics and reproducibility. All samples analyzed were distinct samples. For Ca^{2+} imaging, multiple FDB fibers from each mouse were analyzed but we used nested analyses of fibers from at least three mice of each genotype. Differences between means of two groups were analyzed for significance using Student's t tests and normality tests. If the data failed the normality tests,

we performed a Mann–Whitney rank-sum test. Differences between means of multiple groups were analyzed by one- or two-way ANOVA, and those with multiple individual myofibers per subject were analyzed by nested (hierarchical) ANOVA with Tukey post hoc tests. Mean differences between groups for longitudinal measurements as a function of age are analyzed by repeated measure ANOVA with Tukey post hoc tests. Values of $P < 0.05$ (95% confidence) were considered statistically significant (unless otherwise indicated). Immunoprecipitations were first analyzed for specificity by comparing proteins in IgG controls to those in RyR1 or Jph2 IPs. We used a criterion of $>20\times$ purification and $P < 0.01$. These values were used in the heat maps. However, for discovery proteomic data were analyzed with Holm–Šidáks multiple comparisons tests and/or calculation of the false discovery rate (FDR)⁹⁴. We also used a targeted approach for comparison of the effects of Speg deficiency on known ECC proteins. For comparison of the effects of Speg deficiency the proteins were normalized to the amount of either RyR1 or Jph2 in the IPs and then batch-corrected to the average of the controls samples in each separate experiment. These values are plotted and compared as % control and analyzed by Student's *t* tests and normality tests.

Reporting summary. Further information on research design is available in the Nature Portfolio Reporting Summary linked to this article.

Data availability

Complete datasets from all proteomic studies (Supplementary Data 1) and for Figs. 1–6 (Supplementary Data 2) are provided as supplementary data. All data were generated in the laboratories of Drs. Hamilton, Sung and Rodney. All data in the Supplementary Data Tables and Figs. are in Supplementary Data 3, and all uncropped gels are provided in Supplementary Data 4. The MS data (Supplementary Data 1) have been deposited to the ProteomeXchange Consortium (<https://proteomecentral.proteomexchange.org/>) via the MASSIVE repository (MSV000092796) with the dataset identifier PXD044979. The plasmids for AAV-FKBP12-BirA and AAV-GFP-BirA (complete vector maps in Supplementary Fig. 6) are publicly available through Addgene (ID# 208200 and 208201).

Code availability

Custom routines written in IDL will be made available upon request to George Rodney (Rodney@bcm.edu).

Received: 3 April 2023; Accepted: 7 September 2023;

Published online: 14 September 2023

References

- Gomez-Oca, R., Cowling, B. S. & Laporte, J. Common pathogenic mechanisms in centronuclear and myotubular myopathies and latest treatment advances. *Int. J. Mol. Sci.* **22**. <https://doi.org/10.3390/ijms222111377> (2021).
- Gineste, C. & Laporte, J. Therapeutic approaches in different congenital myopathies. *Curr. Opin. Pharm.* **68**, 102328 (2022).
- Fujise, K., Noguchi, S. & Takeda, T. Centronuclear myopathy caused by defective membrane remodelling of dynamin 2 and BIN1 variants. *Int. J. Mol. Sci.* **23**. <https://doi.org/10.3390/ijms23116274> (2022).
- Lawlor, M. W. & Dowling, J. J. X-linked myotubular myopathy. *Neuromuscul. Disord.* **31**, 1004–1012 (2021).
- Campbell, H., Aguilar-Sanchez, Y., Quick, A. P., Dobrev, D. & Wehrens, X. H. T. SPEG: a key regulator of cardiac calcium homeostasis. *Cardiovasc. Res.* **117**, 2175–2185 (2021).
- Luo, S., Rosen, S. M., Li, Q. & Agrawal, P. B. Striated preferentially expressed protein kinase (SPEG) in muscle development, function, and disease. *Int. J. Mol. Sci.* **22**. <https://doi.org/10.3390/ijms22115732> (2021).
- Hayes, L. H. et al. Phenotypic spectrum of DNM2-related centronuclear myopathy. *Neurol. Genet.* **8**, e200027 (2022).
- Ogasawara, M. & Nishino, I. A review of major causative genes in congenital myopathies. *J. Hum. Genet.* <https://doi.org/10.1038/s10038-022-01045-w> (2022).
- Al-Qusairi, L. et al. T-tubule disorganization and defective excitation-contraction coupling in muscle fibers lacking myotubularin lipid phosphatase. *Proc. Natl. Acad. Sci. USA* **106**, 18763–18768 (2009).
- Luo, S. et al. SPEG binds with desmin and its deficiency causes defects in triad and focal adhesion proteins. *Hum. Mol. Genet.* **29**, 3882–3891 (2021).
- Campbell, H. M. et al. Loss of SPEG inhibitory phosphorylation of ryanodine receptor type-2 promotes atrial fibrillation. *Circulation* **142**, 1159–1172 (2020).
- Quick, A. P. et al. SPEG (striated muscle preferentially expressed protein kinase) is essential for cardiac function by regulating junctional membrane complex activity. *Circ. Res.* **120**, 110–119 (2017).
- Quan, C. et al. SPEG controls calcium reuptake into the sarcoplasmic reticulum through regulating SERCA2a by its second kinase-domain. *Circ. Res.* **124**, 712–726 (2019).
- Agrawal, P. B. et al. SPEG interacts with myotubularin, and its deficiency causes centronuclear myopathy with dilated cardiomyopathy. *Am. J. Hum. Genet.* **95**, 218–226 (2014).
- Li, Q. et al. Dynamin-2 reduction rescues the skeletal myopathy of a SPEG-deficient mouse model. *JCI Insight* **7**. <https://doi.org/10.1172/jci.insight.157336> (2022).
- Kuo, I. Y. & Ehrlich, B. E. Signaling in muscle contraction. *Cold Spring Harb. Perspect. Biol.* **7**, a006023 (2015).
- Caswell, A. H. & Brandt, N. R. Triadic proteins of skeletal muscle. *J. Bioenerg. Biomembr.* **21**, 149–162 (1989).
- Pessah, I. N., Francini, A. O., Scales, D. J., Waterhouse, A. L. & Casida, J. E. Calcium-ryanodine receptor complex. Solubilization and partial characterization from skeletal muscle junctional sarcoplasmic reticulum vesicles. *J. Biol. Chem.* **261**, 8643–8648 (1986).
- Pessah, I. N., Waterhouse, A. L. & Casida, J. E. The calcium-ryanodine receptor complex of skeletal and cardiac muscle. *Biochem. Biophys. Res. Commun.* **128**, 449–456 (1985).
- Rossi, D. et al. Molecular determinants of homo- and heteromeric interactions of Junctophilin-1 at triads in adult skeletal muscle fibers. *Proc. Natl. Acad. Sci. USA* **116**, 15716–15724 (2019).
- Takeshima, H., Hoshijima, M. & Song, L. S. Ca(2+)-microdomains organized by junctophilins. *Cell Calcium* **58**, 349–356 (2015).
- Komazaki, S., Ito, K., Takeshima, H. & Nakamura, H. Deficiency of triad formation in developing skeletal muscle cells lacking junctophilin type 1. *FEBS Lett.* **524**, 225–229 (2002).
- van Oort, R. J. et al. Disrupted junctional membrane complexes and hyperactive ryanodine receptors after acute junctophilin knockdown in mice. *Circulation* **123**, 979–988 (2011).
- Marty, I. Triadin regulation of the ryanodine receptor complex. *J. Physiol.* **593**, 3261–3266 (2015).
- Flucher, B. E. et al. Triad formation: organization and function of the sarcoplasmic reticulum calcium release channel and triadin in normal and dysgenic muscle in vitro. *J. Cell Biol.* **123**, 1161–1174 (1993).
- Oddoux, S. et al. Triadin deletion induces impaired skeletal muscle function. *J. Biol. Chem.* **284**, 34918–34929 (2009).
- Fan, G. C., Yuan, Q., Zhao, W., Chu, G. & Kranias, E. G. Junctin is a prominent regulator of contractility in cardiomyocytes. *Biochem. Biophys. Res. Commun.* **352**, 617–622 (2007).
- Hong, C. S., Kwon, S. J. & Kim, D. H. Multiple functions of junctin and junctate, two distinct isoforms of aspartyl beta-hydroxylase. *Biochem. Biophys. Res. Commun.* **362**, 1–4 (2007).
- Jayaraman, T. et al. FK506 binding protein associated with the calcium release channel (ryanodine receptor). *J. Biol. Chem.* **267**, 9474–9477 (1992).
- Timerman, A. P. et al. The calcium release channel of sarcoplasmic reticulum is modulated by FK-506-binding protein. Dissociation and reconstitution of FKBP-12 to the calcium release channel of skeletal muscle sarcoplasmic reticulum. *J. Biol. Chem.* **268**, 22992–22999 (1993).
- Tang, W. et al. Altered excitation-contraction coupling with skeletal muscle specific FKBP12 deficiency. *FASEB J.* **18**, 1597–1599 (2004).
- Polster, A., Nelson, B. R., Olson, E. N. & Beam, K. G. Stac3 has a direct role in skeletal muscle-type excitation-contraction coupling that is disrupted by a myopathy-causing mutation. *Proc. Natl. Acad. Sci. USA* **113**, 10986–10991 (2016).
- Horstlick, E. J. et al. Stac3 is a component of the excitation-contraction coupling machinery and mutated in Native American myopathy. *Nat. Commun.* **4**, 1952 (2013).
- Campiglio, M. & Flucher, B. E. STAC3 stably interacts through its C1 domain with Ca(V)1.1 in skeletal muscle triads. *Sci. Rep.* **7**, 41003 (2017).
- Brandt, N. R., Caswell, A. H., Brandt, T., Brew, K. & Mellgren, R. L. Mapping of the calpain proteolysis products of the junctional foot protein of the skeletal muscle triad junction. *J. Membr. Biol.* **127**, 35–47 (1992).
- Imagawa, T., Leung, A. T. & Campbell, K. P. Phosphorylation of the 1,4-dihydropyridine receptor of the voltage-dependent Ca²⁺ channel by an

- intrinsic protein kinase in isolated triads from rabbit skeletal muscle. *J. Biol. Chem.* **262**, 8333–8339 (1987).
37. Fuentes, O., Valdivia, C., Vaughan, D., Coronado, R. & Valdivia, H. H. Calcium-dependent block of ryanodine receptor channel of swine skeletal muscle by direct binding of calmodulin. *Cell Calcium* **15**, 305–316 (1994).
 38. Yang, H. C., Reedy, M. M., Burke, C. L. & Strasburg, G. M. Calmodulin interaction with the skeletal muscle sarcoplasmic reticulum calcium channel protein. *Biochemistry* **33**, 518–525 (1994).
 39. Huntoon, V. et al. SPEG-deficient skeletal muscles exhibit abnormal triad and defective calcium handling. *Hum. Mol. Genet.* **27**, 1608–1617 (2018).
 40. Li, Q. et al. Striated preferentially expressed protein kinase (SPEG)-deficient skeletal muscles display fewer satellite cells with reduced proliferation and delayed differentiation. *Am. J. Pathol.* **190**, 2453–2463 (2020).
 41. Qualls, A. E. et al. Novel SPEG mutations in congenital myopathies: genotype-phenotype correlations. *Muscle Nerve* **59**, 357–362 (2019).
 42. Shu, C. et al. Pressure overload in mice with haploinsufficiency of striated preferentially expressed gene leads to decompensated heart failure. *Front. Physiol.* **9**, 863 (2018).
 43. Lu, F. et al. CMYA5 establishes cardiac dyad architecture and positioning. *Nat. Commun.* **13**, 2185 (2022).
 44. Kutchukian, C. et al. Phosphatidylinositol 3-kinase inhibition restores Ca²⁺ release defects and prolongs survival in myotubularin-deficient mice. *Proc. Natl. Acad. Sci. USA* **113**, 14432–14437 (2016).
 45. Reynolds, J. O. et al. Junctophilin-2 is necessary for T-tubule maturation during mouse heart development. *Cardiovasc. Res.* **100**, 44–53 (2013).
 46. Yang, Z. F. et al. Structures of the junctophilin/voltage-gated calcium channel interface reveal hot spot for cardiomyopathy mutations. *Proc. Natl. Acad. Sci. USA* **119**, e2120416119 (2022).
 47. Perni, S. & Beam, K. Junctophilins 1, 2, and 3 all support voltage-induced Ca²⁺ release despite considerable divergence. *J. Gen. Physiol.* **154**. <https://doi.org/10.1085/jgp.202113024> (2022).
 48. Lahiri, S. K. et al. Nuclear localization of a novel calpain-2 mediated junctophilin-2 C-terminal cleavage peptide promotes cardiomyocyte remodeling. *Basic Res. Cardiol.* **115**, 49 (2020).
 49. Wang, J. et al. Calpain-2 specifically cleaves Junctophilin-2 at the same site as Calpain-1 but with less efficacy. *Biochem. J.* **478**, 3539–3553 (2021).
 50. Guo, A. et al. E-C coupling structural protein junctophilin-2 encodes a stress-adaptive transcription regulator. *Science* **362**. <https://doi.org/10.1126/science.aan3303> (2018).
 51. Gross, P. et al. Interaction of the joining region in junctophilin-2 with the L-type Ca(2+) channel is pivotal for cardiac dyad assembly and intracellular Ca(2+) dynamics. *Circ. Res.* **128**, 92–114 (2021).
 52. Poulet, C. et al. Junctophilin-2 tethers T-tubules and recruits functional L-type calcium channels to lipid rafts in adult cardiomyocytes. *Cardiovasc. Res.* **117**, 149–161 (2021).
 53. Stathopoulou, K. et al. CMYA5 is a novel interaction partner of FHL2 in cardiac myocytes. *FEBS J.* <https://doi.org/10.1111/febs.16402> (2022).
 54. Hanke, T., Szawlowski, P. & Randall, R. E. Construction of solid matrix-antibody-antigen complexes containing simian immunodeficiency virus p27 using tag-specific monoclonal antibody and tag-linked antigen. *J. Gen. Virol.* **73**, 653–660 (1992).
 55. Saiz-Baggetto, S., Mendez, E., Quilis, I., Igual, J. C. & Bano, M. C. Chimeric proteins tagged with specific 3xHA cassettes may present instability and functional problems. *PLoS ONE* **12**, e0183067 (2017).
 56. Babcock, L. W., Hanna, A. D., Agha, N. H. & Hamilton, S. L. MyoSight-semi-automated image analysis of skeletal muscle cross sections. *Skelet. Muscle* **10**, 33 (2020).
 57. Niggli, E. Localized intracellular calcium signaling in muscle: calcium sparks and calcium quarks. *Annu. Rev. Physiol.* **61**, 311–335 (1999).
 58. Minamisawa, S. et al. Junctophilin type 2 is associated with caveolin-3 and is down-regulated in the hypertrophic and dilated cardiomyopathies. *Biochem. Biophys. Res. Commun.* **325**, 852–856 (2004).
 59. Zhang, H. B. et al. Ultrastructural uncoupling between T-tubules and sarcoplasmic reticulum in human heart failure. *Cardiovasc. Res.* **98**, 269–276 (2013).
 60. Pinali, C. et al. Post-myocardial infarction T-tubules form enlarged branched structures with dysregulation of junctophilin-2 and bridging integrator 1 (BIN-1). *J. Am. Heart Assoc.* **6**. <https://doi.org/10.1161/JAHA.116.004834> (2017).
 61. Wu, C. Y. et al. Calpain-dependent cleavage of junctophilin-2 and T-tubule remodeling in a mouse model of reversible heart failure. *J. Am. Heart Assoc.* **3**, e000527 (2014).
 62. Weninger, G. et al. Calpain cleavage of Junctophilin-2 generates a spectrum of calcium-dependent cleavage products and DNA-rich NT(1)-fragment domains in cardiomyocytes. *Sci. Rep.* **12**, 10387 (2022).
 63. Piggott, C. A. & Jin, Y. Junctophilins: key membrane tethers in muscles and neurons. *Front. Mol. Neurosci.* **14**, 709390 (2021).
 64. Jiang, M. et al. S-Palmitoylation of junctophilin-2 is critical for its role in tethering the sarcoplasmic reticulum to the plasma membrane. *J. Biol. Chem.* **294**, 13487–13501 (2019).
 65. Guo, A. et al. Molecular determinants of calpain-dependent cleavage of junctophilin-2 protein in cardiomyocytes. *J. Biol. Chem.* **290**, 17946–17955 (2015).
 66. Hein, M. Y. et al. A human interactome in three quantitative dimensions organized by stoichiometries and abundances. *Cell* **163**, 712–723 (2015).
 67. Oostdyk, L. T. et al. Towards improving proximity labeling by the biotin ligase BirA. *Methods* **157**, 66–79 (2019).
 68. Lee, C. S. et al. Ligands for FKBP12 increase Ca²⁺ influx and protein synthesis to improve skeletal muscle function. *J. Biol. Chem.* **289**, 25556–25570 (2014).
 69. Zalk, R. & Marks, A. R. Ca(2+) release channels join the ‘resolution revolution’. *Trends Biochem. Sci.* **42**, 543–555 (2017).
 70. Melville, Z., Kim, K., Clarke, O. B. & Marks, A. R. High-resolution structure of the membrane-embedded skeletal muscle ryanodine receptor. *Structure* **30**, 172–180 e173 (2022).
 71. des Georges, A. et al. Structural basis for gating and activation of RyR1. *Cell* **167**, 145–157 e117 (2016).
 72. Chiang, D. Y. et al. Impaired local regulation of ryanodine receptor type 2 by protein phosphatase 1 promotes atrial fibrillation. *Cardiovasc. Res.* **103**, 178–187 (2014).
 73. Fukuzawa, A. et al. Interactions with titin and myomesin target obscurin and obscurin-like 1 to the M-band: implications for hereditary myopathies. *J. Cell Sci.* **121**, 1841–1851 (2008).
 74. Lange, S. et al. Obscurin determines the architecture of the longitudinal sarcoplasmic reticulum. *J. Cell Sci.* **122**, 2640–2650 (2009).
 75. Benson, M. A. et al. Ryanodine receptors are part of the myospryn complex in cardiac muscle. *Sci. Rep.* **7**, 6312 (2017).
 76. Chiang, D. Y. et al. Phosphorylation-dependent interactome of ryanodine receptor type 2 in the heart. *Proteomes* **9**. <https://doi.org/10.3390/proteomes9020027> (2021).
 77. Pierantozzi, E. et al. Impaired intracellular Ca(2+) dynamics, M-band and sarcomere fragility in skeletal muscles of obscurin KO mice. *Int. J. Mol. Sci.* **23**. <https://doi.org/10.3390/ijms23031319> (2022).
 78. Sarparanta, J. et al. Interactions with M-band titin and calpain 3 link myospryn (CMYA5) to tibial and limb-girdle muscular dystrophies. *J. Biol. Chem.* **285**, 30304–30315 (2010).
 79. Reynolds, J. G., McCalmon, S. A., Donaghey, J. A. & Naya, F. J. Deregulated protein kinase A signaling and myospryn expression in muscular dystrophy. *J. Biol. Chem.* **283**, 8070–8074 (2008).
 80. Yao, W. et al. Activation of esterase D by FPD5 inhibits growth of A549 lung cancer cells via JAB1/p53 pathway. *Genes* **13**. <https://doi.org/10.3390/genes13050786> (2022).
 81. Lanza, D. G. et al. Comparative analysis of single-stranded DNA donors to generate conditional null mouse alleles. *BMC Biol.* **16**, 69 (2018).
 82. Burrage, L. C. et al. Bi-allelic variants in TONSL cause SPONASTRIME dysplasia and a spectrum of skeletal dysplasia phenotypes. *Am. J. Hum. Genet.* **104**, 422–438 (2019).
 83. Stroup, B. M. et al. A global Slc7a7 knockout mouse model demonstrates characteristic phenotypes of human lysinuric protein intolerance. *Hum. Mol. Genet.* **29**, 2171–2184 (2020).
 84. Marom, R. et al. COPB2 loss of function causes a coatopathy with osteoporosis and developmental delay. *Am. J. Hum. Genet.* **108**, 1710–1724 (2021).
 85. Hanna, A. D. et al. Pathological mechanisms of vacuolar aggregate myopathy arising from a Casq1 mutation. *FASEB J.* **35**, e21349 (2021).
 86. Pal, R. et al. Src-dependent impairment of autophagy by oxidative stress in a mouse model of Duchenne muscular dystrophy. *Nat. Commun.* **5**, 4425 (2014).
 87. Rodney, G. G. Calmodulin in adult mammalian skeletal muscle: localization and effect on sarcoplasmic reticulum Ca²⁺ release. *Am. J. Physiol. Cell Physiol.* **294**, C1288–C1297 (2008).
 88. Guo, A. & Song, L. S. AutoTT: automated detection and analysis of T-tubule architecture in cardiomyocytes. *Biophys. J.* **106**, 2729–2736 (2014).
 89. Xiao, X., Li, J. & Samulski, R. J. Production of high-titer recombinant adeno-associated virus vectors in the absence of helper adenovirus. *J. Virol.* **72**, 2224–2232 (1998).
 90. Lagor, W. R., Johnston, J. C., Lock, M., Vandenbergh, L. H. & Rader, D. J. Adeno-associated viruses as liver-directed gene delivery vehicles: focus on lipoprotein metabolism. *Methods Mol. Biol.* **1027**, 273–307 (2013).
 91. Karki, M. et al. A cytoskeletal function for PBRM1 reading methylated microtubules. *Sci. Adv.* **7**. <https://doi.org/10.1126/sciadv.abf2866> (2021).
 92. Rappsilber, J., Ishihama, Y. & Mann, M. Stop and go extraction tips for matrix-assisted laser desorption/ionization, nanoelectrospray, and LC/MS sample pretreatment in proteomics. *Anal. Chem.* **75**, 663–670 (2003).

93. Saltzman, A. B. et al. gpGrouper: a peptide grouping algorithm for gene-centric inference and quantitation of bottom-up proteomics data. *Mol. Cell Proteom.* **17**, 2270–2283 (2018).
94. Gujar, H., Liang, J. W., Wong, N. C. & Mozhui, K. Profiling DNA methylation differences between inbred mouse strains on the Illumina Human Infinium MethylationEPIC microarray. *PLoS ONE* **13**, e0193496 (2018).

Acknowledgements

We thank the directors and staff at the Genetically Engineered Rat and Mouse Core, the Mouse Metabolism and Phenotyping Core, the Optical Imaging and Vital Microscopy Cores at BCM and the Genetically Engineered Rodent Model (GERM) Core at BCM. We would also like to thank Dr. Robert Dirksen for sharing the design of the vector for the V5/HA-tag, and Drs. Ang Guo and Long-Sheng Song (University of Iowa Carver College) for supplying the AutoTT program. High-resolution X-ray microtomography was conducted in the Optical Imaging and Vital Microscopy Core at BCM, and echocardiography was conducted at the Mouse Metabolism and Phenotyping Core at Baylor College of Medicine. The Mouse Metabolism and Phenotyping Core is supported by RO1DK114356, UM1HG006348, and S10OD032380. The GERM Core is funded in part by the National Institutes of Health Cancer Center Grant (P30 CA125123). Research reported in this publication was supported by R01AR072475 to S.L.H., R01 HL132840 and R01 DK124477 to W.R.L., R01-HL089598, R01-147108, R01-HL153350 to X.H.T.W., and R01AR061370 NIH/NIAMS to G.G.R.

Author contributions

All authors helped with the writing of the manuscript, read, critiqued, and corrected multiple versions of the manuscript, and approved the last version. C.S.L. performed and analyzed data from western blotting, Jph2 fragmentation, and immunoprecipitations, helped supervise students, and performed the multiple aspects of the study. S.Y.J. performed and analyzed proteomic data, R.S.Z.Y. performed and analyzed in vivo analyses of growth and body composition and analyzed mRNA levels for Speg isoforms, N.H.A. collected and analyzed t-tubule structure in FDB fibers and handled the mouse matings, J.H. performed and analyzed the BioID experiments, T.C. performed and analyzed cardiac echoes, L.B. performed and analyzed force-frequency studies and CSA/fiber-type distribution analyses, J.D.F. performed and analyzed Jph2 fragmentation studies, B.C. performed and analyzed force-frequency data, A.D.H. performed and analyzed force-frequency and echo data, C.S.W. supervised all in vivo mouse studies and optimized the echoes, D.L. created HA-Speg mice, A.E.H. prepared the AAV for the BioID experiments, P.Z. created the BioID targeting vectors, X.H.T.W. suggested experiments for the revision, critiqued the ms, and helped write the revision, WRL designed, created, and supervised the AAV vector studies, G.G.R. helped plan the study, supervised the force experiments and performed and analyzed the Ca²⁺ sparks and t-tubule studies, S.L.H.

supervised the entire study, planned the experiments, analyzed data, created the figures, and wrote the first and last versions of the manuscript.

Competing interests

The authors declare the following competing interests: X.H.T.W. is a founding partner and board member of Elex Biotech, a start-up company that developed drug molecules to target ryanodine receptors to treat cardiac arrhythmias. The remaining authors declare no competing interests.

Additional information

Supplementary information The online version contains supplementary material available at <https://doi.org/10.1038/s42003-023-05330-y>.

Correspondence and requests for materials should be addressed to Susan L. Hamilton.

Peer review information *Communications Biology* thanks Cecilia Hidalgo and the other, anonymous, reviewer(s) for their contribution to the peer review of this work. Primary Handling Editors: Alexander Cartagena-Rivera and Joao Valente. A peer review file is available.

Reprints and permission information is available at <http://www.nature.com/reprints>

Publisher's note Springer Nature remains neutral with regard to jurisdictional claims in published maps and institutional affiliations.



Open Access This article is licensed under a Creative Commons Attribution 4.0 International License, which permits use, sharing, adaptation, distribution and reproduction in any medium or format, as long as you give appropriate credit to the original author(s) and the source, provide a link to the Creative Commons licence, and indicate if changes were made. The images or other third party material in this article are included in the article's Creative Commons licence, unless indicated otherwise in a credit line to the material. If material is not included in the article's Creative Commons licence and your intended use is not permitted by statutory regulation or exceeds the permitted use, you will need to obtain permission directly from the copyright holder. To view a copy of this licence, visit <http://creativecommons.org/licenses/by/4.0/>.

© The Author(s) 2023